Diplomarbeit

Fluid Dynamics in the Human Upper Airways

ausgeführt zum Zwecke der Erlangung des akademischen Grades eines Diplom-Ingenieurs (Dipl.-Ing. oder DI), eingereicht an der TU Wien, Fakultät für Maschinenwesen und Betriebswissenschaften, von

Maximilian KREXNER

Mat.Nr.: 01528948
Bruno-Marek-Allee 18/72, 1020 Wien, Austria

unter der Leitung von
Privatdoz. Francesco Zonta, MSc PhD
Institut für Strömungsmechanik und Wärmeübertragung, E322

Wien, Jänner 2023

TU WIEN Bibliothek Your knowledge hub
Die approbierte gedruckte Originalversion dieser Diplomarbeit ist an der TU Wien Bibliothek verfügbar
The approved original version of this thesis is available in print at TU Wien Bibliothek.

Ich nehme zur Kenntnis, dass ich zur Drucklegung dieser Arbeit nur mit Bewilligung der Prüfungskommission berechtigt bin.

Eidesstattliche Erklärung

Ich erkläre an Eides statt, dass die vorliegende Arbeit nach den anerkannten Grundsätzen für wissenschaftliche Abhandlungen von mir selbstständig erstellt wurde. Alle verwendeten Hilfsmittel, insbesondere die zugrunde gelegte Literatur, sind in dieser Arbeit genannt und aufgelistet. Die aus den Quellen wörtlich entnommenen Stellen, sind als solche kenntlich gemacht.

Das Thema dieser Arbeit wurde von mir bisher weder im In- noch Ausland einer Beurteilerin/einem Beurteiler zur Begutachtung in irgendeiner Form als Prüfungsarbeit vorgelegt. Diese Arbeit stimmt mit der von den Begutachterinnen/Begutachtern beurteilten Arbeit überein.

Ich nehme zur Kenntnis, dass die vorgelegte Arbeit mit geeigneten und dem derzeitigen Stand der Technik entsprechenden Mitteln (Plagiat-Erkennungssoftware) elektronisch-technisch überprüft wird. Dies stellt einerseits sicher, dass bei der Erstellung der vorgelegten Arbeit die hohen Qualitätsvorgaben im Rahmen der geltenden Regeln zur Sicherung guter wissenschaftlicher Praxis „Code of Conduct“ an der TU Wien eingehalten wurden. Zum anderen werden durch einen Abgleich mit anderen studentischen Abschlussarbeiten Verletzungen meines persönlichen Urheberrechts vermieden.

Stadt und Datum		*Unterschrift*

Die approbierte gedruckte Originalversion dieser Diplomarbeit ist an der TU Wien Bibliothek verfügbar
The approved original version of this thesis is available in print at TU Wien Bibliothek.
TU WIEN Bibliothek Your knowledge hub

Kurzfassung

Noch nie war es so klar wie in dieser Zeit, dass die Strömungsdynamik, insbesondere die Tröpfchendynamik, unser tägliches Leben beeinflusst. In der Luft befindliche Tröpfchen und Aerosole, die der Mensch beim Niesen, Husten oder Atmen produziert, können Atemwegsviren (wie SARS-CoV-2) übertragen und die Infektionsrate vor allem in geschlossenen Umgebungen/Räumen erheblich erhöhen. Tröpfchen werden auch als Therapiemittel zur Unterdrückung von Infektionen und Erkrankungen der oberen Atemwege eingesetzt, indem natürliche Thermalwässer mit unterschiedlichen Eigenschaften und Zusammensetzungen in die Nasenhöhle eingeatmet werden.

In all diesen Fällen lauten die Schlüsselfragen: Wie weit gelangen die Tropfen in die Luftwege des Atmungssystems? Was bewirken sie, wenn sie sich absetzen? Und wann lagern sie sich ab? Die Antworten auf diese Fragen hängen natürlich von der Größe, der Form, der Dichte und der chemischen Zusammensetzung der Tropfen ab.

In dieser Arbeit versuchen wir diese Fragen zu beantworten, indem wir strömungsmechanische Simulationen für die menschliche Nase mit Hilfe zweier realistischer Geometrien durchführen, die aus Magnetresonanzbildern stammen. Die Simulationen werden für verschiedene Werte der Strömungsgeschwindigkeit des Luftstromes und des Tropfendurchmessers durchgeführt.

Die Ergebnisse zeigen die Gesamteffizienz der menschlichen Nase beim Auffangen von Tropfen und Partikeln.

Schlüsselwörter: Strömungsmechanik, *CFD*, Partikelverfolgung, Naseninnenräume, *OpenFOAM*, Nasenströmung, Ablagerungsrate, Partikelablagerung

Abstract

Never has it been clear as in this moment that fluid dynamics in particular drops dynamics influences our everyday life. Airborne droplets and aerosols produced by humans during a sneeze, cough or breath can carry respiratory viruses (like SARS-CoV-2) and can significantly increase infection rates in particular in closed environments/spaces. Droplets are also used as therapy agents to suppress infections and disorders of the upper respiratory tract, via inhalation in the nasal cavity of natural thermal waters with different characteristics and composition.

In all these cases, the key questions are: How far do drops get in the air passages of the respiratory system? What do they do when they are deposited? And when do they deposit? Naturally, the answers to these questions do depend on drops size, shape, density and chemical composition/nature.

In this thesis we try to answer these questions by performing fluid dynamics simulations of the human nose for two realistic geometries, taken from magnetic resonance images. Simulations are run for different values of the fluid velocity and of the drop diameter.

Results demonstrate the overall efficiency of the human nose in capturing drops and particles.

Keywords: Fluid mechanics, *CFD*, Particle tracking, Nasal interiors, *OpenFOAM*, Nasal flow, Deposition rate, Particle deposition

TU Bibliothek WIEN Your knowledge hub
Die approbierte gedruckte Originalversion dieser Diplomarbeit ist an der TU Wien Bibliothek verfügbar
The approved original version of this thesis is available in print at TU Wien Bibliothek.

Contents

1. Introduction and Motivation 1
2. Nasal Cavity 3
    2.1 Respiratory System 3
    2.2 Anatomy 4
    2.3 Physiology 6
    2.4 Nasal Particle Tracking 7
3. Governing Equations 9
    3.1 Navier-Stokes equations 9
    3.2 RANS – Reynolds averaged Navier-Stokes equations 9
    3.3 k-ω SST Model 10
    3.4 Flow Simulation 11
    3.5 Particle Tracking 11
        3.5.1 Particle Equations 11
        3.5.2 Drag 12
        3.5.3 Particle Stress 13
4. General Simulation Setup 14
    4.1 Geometry 14
    4.2 Mesh Generation 16
        4.2.1 BlockMesh 16
        4.2.2 SnappyHexMesh 16
        4.2.3 Mesh 18
5. Flow Simulation 20
    5.1 Setup 20
    5.2 Results 22
        5.2.1 Test object A 22
        5.2.2 Test object B 26
6. Particle Tracking Simulation 31
    6.1 Setup 31
    6.2 Results 34
7. Analysis 38
    7.1 Flow – Test object A 38
    7.2 Flow – Test object B 38
    7.3 Particle Tracking – Test object A 40
        7.3.1 Nasal Interiors 42
        7.3.2 Nasal Subdivision 47

7.4 Particle Tracking – Test object B 50

7.5 Comparison of test object A and B.. 54

8. Conclusion 55

Bibliography.. 56

List of Figures

Figure 1: Respiratory system [5] 3
Figure 2: Nasal cavity – main bones and cartilages [5] 4
Figure 3: Sliced nasal cavity model; Black – flow area [7] 5
Figure 4: Nasal valve [5] 5
Figure 5: Cross sectional area of the cavity model in figure 3; Top curve – total area, Bottom curves – left and right cavity paths; Area as a function of the distance measured from the nostrils. [7] 5
Figure 6: Nasal cavity – turbinates [8] 6
Figure 7: Deposition efficiency of two replicas of the nasal cavity [1] 8
Figure 8: Test object A: Left – upper nasal airways, right – upper nasal airways with sphere 14
Figure 9: Test object B: Left – head with upper nasal airways, right – corresponding negative image 15
Figure 10: Test object B: Left – relevant geometry, right – geometry after cleaning, general and local smoothing 15
Figure 11: Test object B: Left – upper nasal airways, right – upper nasal airways with sphere 16
Figure 12: SnappyHexMesh; Left - STL surface, Right - cell splitting and background mesh [18] 17
Figure 13: SnappyHexMesh; Cell removal process [18] 17
Figure 14: SnappyHexMesh; Snapping process [18] 18
Figure 15: Main slice of the mesh – test object A 18
Figure 16: Mesh detail – outlet – test object A 19
Figure 17: Main slice of the mesh – test object B 19
Figure 18: Test object A – regions: Grey - outlet, red – wall, green – inlet 20
Figure 19: Test object B – regions: Grey – outlet, red – wall; green – inlet 20
Figure 20: Velocity magnitude in m/s – 5 l/min – test object A 23
Figure 21: Velocity X-component in m/s – 5 l/min – test object A 23
Figure 22: Velocity Y-component in m/s – 5 l/min – test object A 24
Figure 23: Velocity Z-component in m/s – 5 l/min – test object A 24
Figure 24: Velocity magnitude – 10 l/min – test object A 25
Figure 25: Velocity magnitude – 15 l/min – test object A 25
Figure 26: Velocity magnitude – 20 l/min – test object A 25
Figure 27: Velocity magnitude – 5 l/min – test object B – main section 26
Figure 28: Velocity magnitude – 10 l/min – test object B – main section 26
Figure 29: Velocity magnitude – 15 l/min – test object B – main section 27
Figure 30: Velocity magnitude – 20 l/min – test object B – main section 27
Figure 31: Velocity magnitude – 60 l/min – test object B – main section 27
Figure 32: Velocity magnitude – 120 l/min – test object B – main section 28
Figure 33: Velocity magnitude – 5 l/min – test object B – throat 28
Figure 34: Velocity magnitude – 20 l/min – test object B – throat 28
Figure 35: Velocity magnitude – 60 l/min – test object B – throat 29
Figure 36: Velocity magnitude – 120 l/min – test object B – throat 29
Figure 37: Velocity magnitude – 5 l/min – test object B – turbinates 29
Figure 38: Velocity magnitude – 20 l/min – test object B – turbinates 30
Figure 39: Velocity magnitude – 60 l/min – test object B – turbinates 30
Figure 40: Velocity magnitude – 60 l/min – test object B – turbinates 30
Figure 41: Particle Tracking – 1 µm and 5 l/min – test object A: Red – active (travelling) particles, blue – inactive (stuck) particles 34
Figure 42: Particle Tracking – 50 µm and 15 l/min – test object A: Red – active (travelling) particles, blue – inactive (stuck) particles 35

Figure 43: Particle Tracking 10 µm and 20 l/min – test object A: Red – active (travelling) particles, blue – inactive (stuck) particles 35
Figure 44: Particle Tracking – 1 µm and 5 l/min – test object B: Red – active (travelling) particles, blue – inactive (stuck) particles 36
Figure 45: Particle Tracking – 30 µm and 20 l/min – test object B: Red – active (travelling) particles, blue – inactive (stuck) particles 36
Figure 46: Particle Tracking – 20 µm and 5 l/min – test object B: Red – active (travelling) particles, blue – inactive (stuck) particles 37
Figure 47: Pressure drop – test object A 38
Figure 48: Pressure drop – test object A 39
Figure 49: Blue – nasal interiors, green – throat, red – nasal cavity 40
Figure 50: Deposition fraction in dependence of the impaction parameter for different flowrates with indication of the particle sizes – test object A 43
Figure 51: Deposition fraction in dependence of the particle diameter for different flowrates – test object A 43
Figure 52: Deposition fraction – approximation – test object A 44
Figure 53: Deposition fraction – comparison – test object A 45
Figure 54: Deposition fraction in dependence of the squared particle diameter times the pressure drop for different flowrates with indication of the particle sizes – test object A 46
Figure 55: Deposition fraction – 1 µm – test object A 47
Figure 56: Deposition fraction – 5 µm – test object A 48
Figure 57: Deposition fraction – 10 µm – test object A 48
Figure 58: Deposition fraction – 20 µm – test object A 49
Figure 59: Deposition fraction – 30 µm – test object A 49
Figure 60: Deposition fraction – 50 µm – test object A 50
Figure 61: Blue – nasal interiors – test object B 50
Figure 62: Deposition fraction in dependence of the impaction parameter for different flowrates with indication of the particle sizes – test object B 52
Figure 63: Deposition fraction in dependence of the particle diameter for different flowrates – test object B 53
Figure 64: Deposition fraction in dependence of the squared particle diameter times the pressure drop for different flowrates with indication of the particle sizes – test object B 53

List of Tables

Table 1: Pressure drop 39
Table 2: Main data for the particle tracking of test object A 41
Table 3: Main data for the particle tracking of test object B 51

List of Acronyms

CFD	Computational fluid dynamic
DF	Deposition fraction
IP	Impaction parameter
MPPIC	Multiphase particle in cell method
MRT	Magnetic resonance tomography
RANS	Reynolds averaged Navier-Stokes equations
SOI	Start of injection
STL	Stereolithography

1. Introduction and Motivation

The understanding and knowledge of the physiology and anatomy of the human nasal airways is essential to deal with increasingly important problems. Understanding about the fluid dynamical characteristics can contribute to solve many human problems or form the basis for further studies. In particular, the knowledge about the ability of particles travelling through the human upper airways and of their deposition is essential for numerous applications and processes. In the following some examples are explained.

The Covid-19 crisis showed how easily a disease, especially small virus particles, can block an entire society. Based on knowledge of how small virus particles enter the respiratory system, particularly via the nose, new methods can swiftly be developed in order to counter pathogens.

In many working areas there is a considerable dust load, for example in construction zones, carpentry shops, or the dust load of flour at bakeries. This dust pollution is toxic for workers and can lead to serious health problems. So, any information on how particles enter the nose or respiratory system and where they deposit can help to prevent serious problems from further occurring.

A similar problem is well known to people who suffer from allergies. The knowledge about particle deposition in the nose could be used to reduce the pollen pollution and lead to an improved quality of life.

A technical application that could be improved by applying the knowledge of fluid dynamics on the human upper airways are nasal sprays. These could be designed in a way that they deliver drugs in the most efficient way to specific regions in the nasal interiors.

Numerous studies have already been conducted on particle deposition in human upper airways. Experiments were executed with replicas of human nasal airways [1]. The results show a significant dependence of the particle deposition on certain parameters. (Further details are described in chapter 2.)

A computational study on micro-particle tracking with a *Lagrangian* model [2] was carried out and showed similar results compared to the experiment mentioned before. Moreover, a study on the flow and the micro-particle deposition again with a *Lagrangian* approach for different nasal cavities was carried out in [3].

Furthermore, research on micro-particle deposition in the human respiratory system during sniffing was conducted [4] by applying a *Lagrangian* approach.

The aim of this thesis is to obtain a greater understanding of the particle flow and deposition through the human upper airways to gain knowledge about the nasal airways and to contribute to further studies. For this purpose, the computational fluid dynamics program *OpenFOAM* and a *Euler-Lagrangian* approach was used for the particle tracking.

The thesis is structured as follows: In chapter 2 basic knowledge on the human nose, the respiratory system and particle tracking is described. For further information, the corresponding literature is quoted. In addition, the governing equations are discussed and explained. Afterwards, the preparation of the corresponding *STL* files and the generation of the mesh are described. The simulations were carried out with two different nasal geometries and following that, the flow simulation is described. After this pre-work the main part on particle tracking is described. In the end, the analysis of the simulations followed by conclusion are presented.

2. Nasal Cavity

The nasal cavity is a complex part of the human body. Basic knowledge must be provided in order to be able to describe the physical processes of it by a technical approach. For further details, consult the corresponding literature. At the end of this chapter, as mentioned in the introduction, basic knowledge about particle tracking is provided.

2.1 Respiratory System

The respiratory system is separated in a conducting and a respiratory zone (figure 1). The inhaled air enters the system either through nose or mouth and passes through the different regions (figure 1) to the alveoli. There the gas exchange takes place. Oxygen is delivered to the cells and carbon dioxide is exhaled. [5]

The nasal cavity is one of the first parts of the conducting system in which inhaled air has to pass.

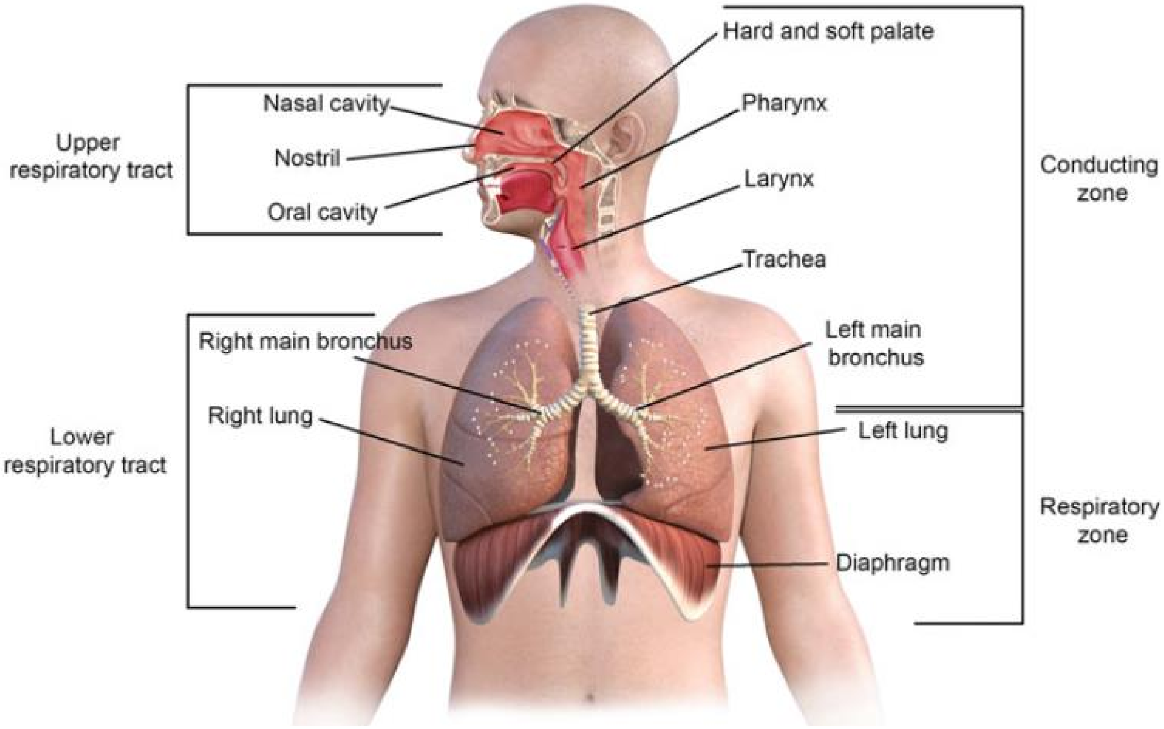
Upper respiratory tract
Nasal cavity
Nostril
Oral cavity
Hard and soft palate
Pharynx
Larynx
Trachea
Conducting zone
Right main bronchus
Right lung
Lower respiratory tract
Left main bronchus
Left lung
Diaphragm
Respiratory zone

Figure 1: Respiratory system [5]

2.2 Anatomy

The nasal airways are approximately 10 cm long and 5 cm high. [6] The nasal septum separates (figure 2) the cavity into a right and a left cavity. [5]

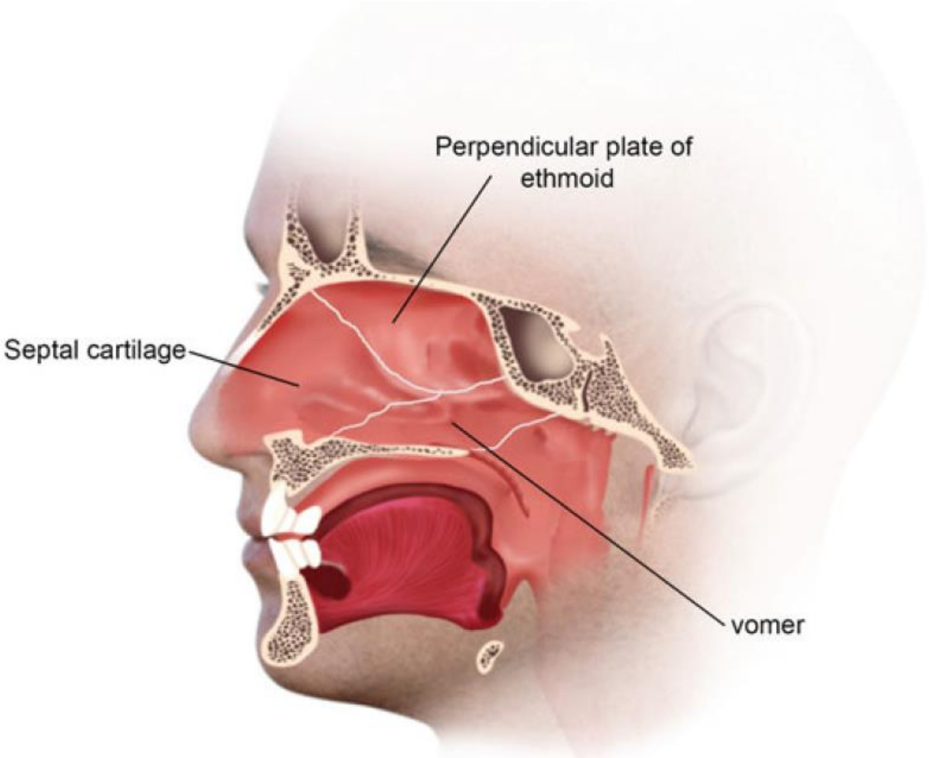

Figure 2: Nasal cavity – main bones and cartilages [5]

The volume which the inhaled air streams through is quite complex. For a better imagination, figure 3 shows a sliced nasal cavity model by an *MRT* scan.

The flow starts vertically and enters the nose through the external nasal valves. As seen in figure 3 the two nostril channels develop to small branches, which entwine around the nasal turbinates. [7] The three turbinates (figure 4) are called inferior, middle and superior turbinate, of which the inferior turbinate is supposed to have the biggest influence on the nasal airflow. [5]

In this region, called meatus nasalis, the flow already changes to a horizontal direction. The straight length of this section is about 40 mm long. In section C (figure 3) the branched channels transform to one single channel - the throat. [7]

In figure 5 the cross sectional area of the nasal airways can be seen. The total area of the main nasal cavity ranges from around 280 to 420 mm^2. Only the nostrils in the beginning and the throat in the end have a smaller area. Moreover, in section C, where the two branches transform to one path, a maximum cross sectional area of about 520 mm^2 can be made out. [7]

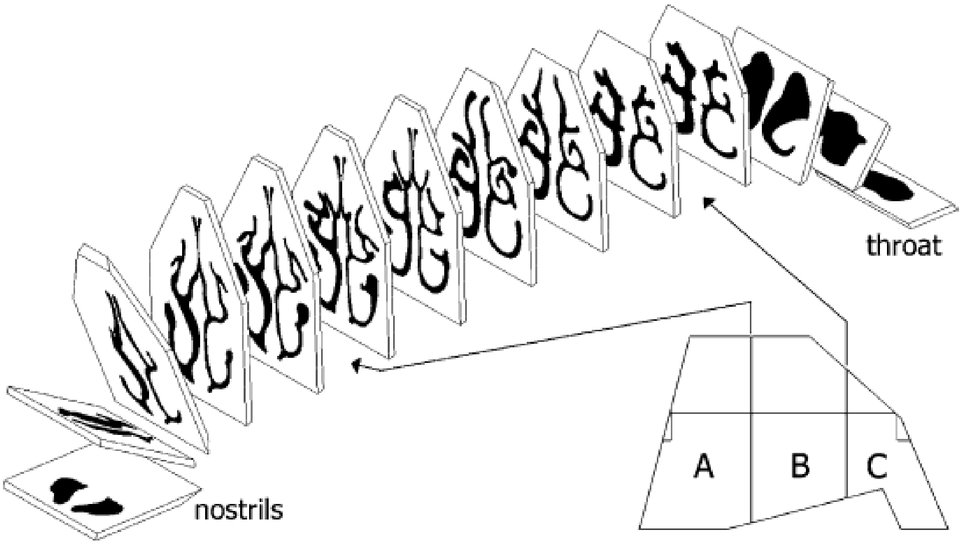
throat
nostrils
A
B
C

Figure 3: Sliced nasal cavity model; Black – flow area [7]

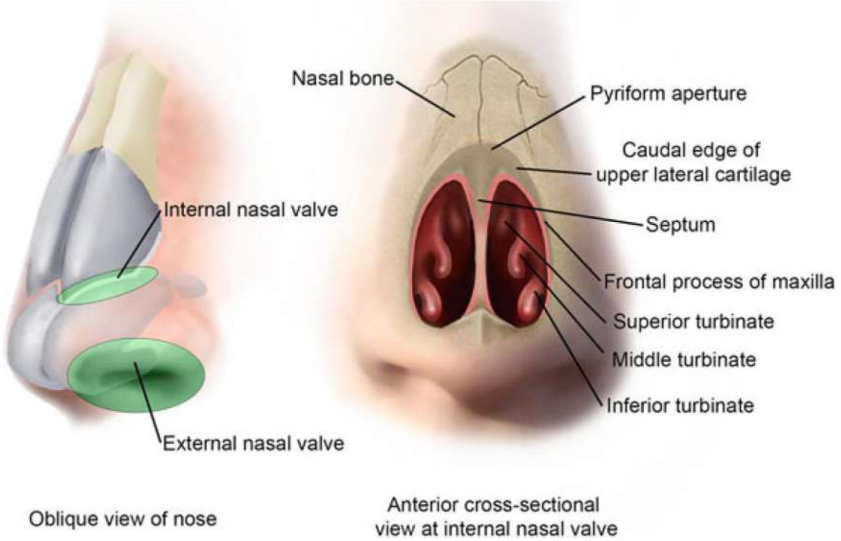
Nasal bone
Pyriform aperture
Caudal edge of upper lateral cartilage
Internal nasal valve
Septum
Frontal process of maxilla
Superior turbinate
Middle turbinate
Inferior turbinate
External nasal valve
Oblique view of nose
Anterior cross-sectional view at internal nasal valve

Figure 4: Nasal valve [5]

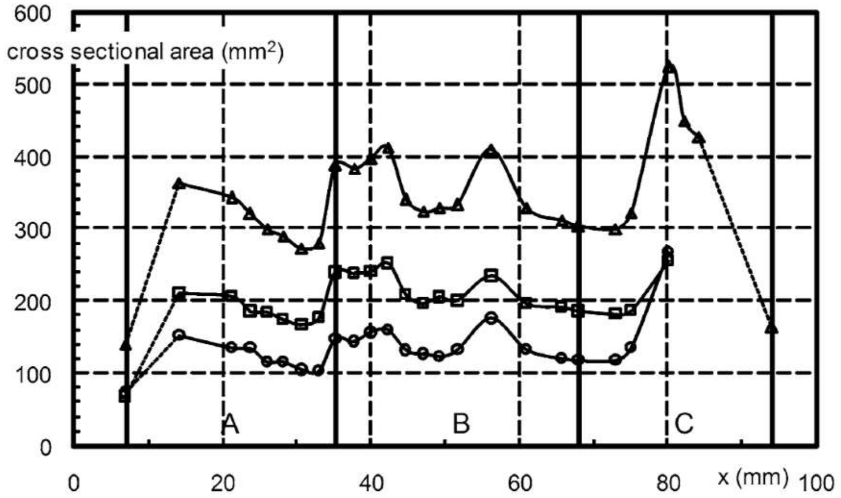

Figure 5: Cross sectional area of the cavity model in figure 3; Top curve – total area, Bottom curves – left and right cavity paths; Area as a function of the distance measured from the nostrils. [7]

2.3 Physiology

The nose and the whole respiratory system of an adult have to process 10^5 litres of air per day. [8]

The main functions of the nose are to warm, clean and humidify the inhaled air. Moreover, it contains several other defence mechanisms, like a changing passage size. All of this is necessary to protect the tissues of the lung. Furthermore, an amount of the inhaled air is lead to sensory receptors, where odorant molecules are captured. [6]

To prevent particles from entering the respiratory system an initial filtration occurs at the nasal hair. Moreover, the complex geometry, like the anatomy of the turbinates in which the air flow has to pass, leads to a deposition in the mucous blanket, where the immune system is able to interact with the foreign bodies. [7]

As previously mentioned, the inhaled air has to be heated and humidified. The nasal mucosa provides a relative humidity of about 95% and maintains a temperature of 31-37°C. The main airflow from nose to pharynx is situated between the middle and the inferior turbinate (figure 6). [8]

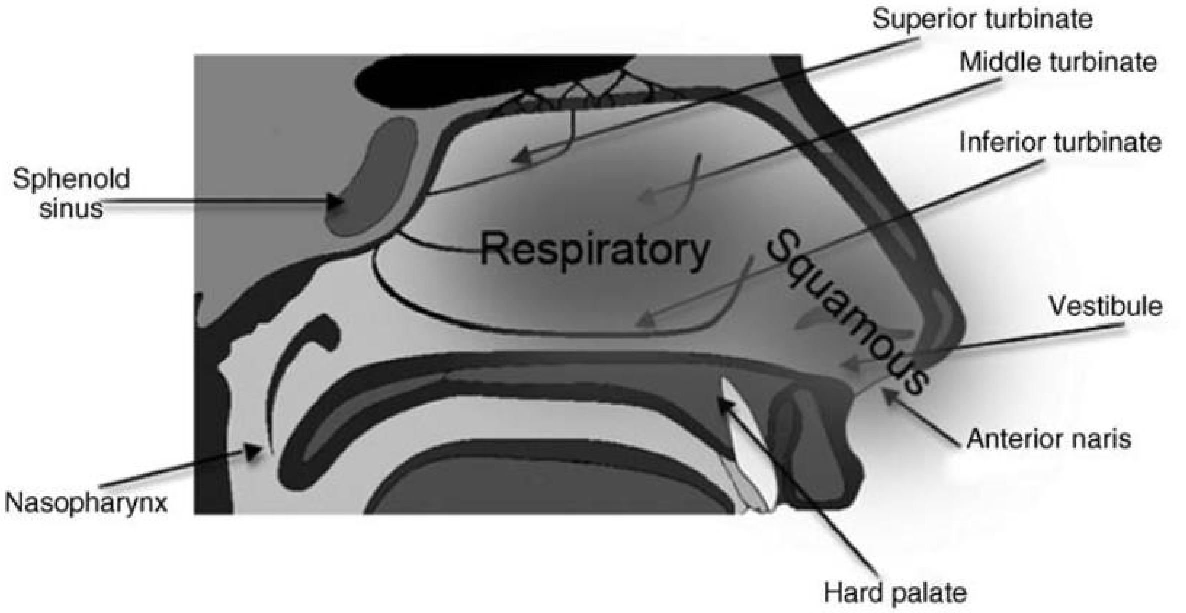
Superior turbinate
Middle turbinate
Inferior turbinate
Sphenold sinus
Respiratory
Squamous
Vestibule
Anterior naris
Nasopharynx
Hard palate

Figure 6: Nasal cavity – turbinates [8]

2.4 Nasal Particle Tracking

The behaviour of micro particle deposition in the nasal cavity up to the nasopharynx was explored in [1] through an experiment with nasal airway replicas. The most important key figures for the micro particle deposition are the impaction parameter, which represents the particle inertia and the deposition efficiency or deposition fraction.

Impaction parameter (IP) [2]

$$IP\left[\frac{\mu m^2 cm^3}{s}\right] = \mathrm{d}_p^2 \cdot Q \tag{1}$$

Deposition efficiency/ Deposition fraction (DF) [2]

$$DF_i = \frac{number\ of\ particles\ depositing\ in\ region\ i}{number\ of\ particles\ entering\ the\ geometry\ inlet} \tag{2}$$

Whereby d_p represents the particle diameter and Q the inhaled volume flow rate. [2]

According to [1] an impaction parameter smaller than about 2000 $\mu m^2 cm^3 s^{-1}$ indicates particles with low inertia. Consequently, they need only a short period of time to adjust their velocity to new conditions of forces. So, particles with small inertia can be easily carried by flow streams through complex geometries. In contrast to this, particles with large inertia, more than about 25000 $\mu m^2 cm^3 s^{-1}$ tend to deviate from flow streamlines, because they have a large relaxation time, meaning that they need more time to adjust their velocity to new conditions of forces. [1] Hence, particles with large inertia are more likely to leave streamlines and deposit in the nasal airways.

In figure 7 the deposition efficiency of [1] in dependence of the impaction parameter is shown. The range of 2000 to 25000 $\mu m^2 cm^3 s^{-1}$ describes a domain, where inertial effects are neither small enough nor big enough. Therefore, the behaviour of the particles is hard to predict and depends on flow features. The differences of the deposition efficiency of the two models (figure 7) results from differences in surface roughness and dimensional tolerances. [1]

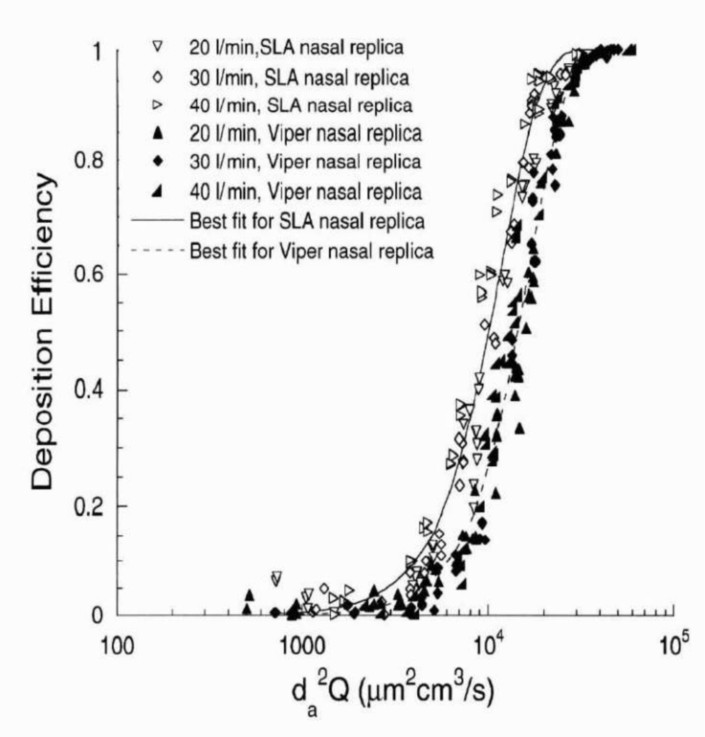

Figure 7: Deposition efficiency of two replicas of the nasal cavity [1]

Other studies show similar curves for the deposition efficiency in the nasal cavity. The different boundaries result in curves, which are similar to figure 7, but moved to smaller or larger impaction parameters ([1], [2]).

3. Governing Equations

In fluid mechanics the three main equations are the conservation laws of momentum, mass and energy. For further information consult the corresponding literature [9]. With the help of the three main equations, the *Navier-Stokes e*quations can be derived.

3.1 Navier-Stokes equations

An important set of equations are the *Navier-Stokes* equations for the incompressible, isothermal flow of *Newtonian* fluids [9].

$$\boldsymbol{\nabla} \cdot \boldsymbol{u} = 0 \tag{3}$$

$$\rho \left[\frac{\partial \boldsymbol{u}}{\partial t} + \boldsymbol{\nabla} \cdot (\boldsymbol{u}\boldsymbol{u}) \right] = -\boldsymbol{\nabla} p + \eta \boldsymbol{\nabla} \cdot (\boldsymbol{\nabla} \mathbf{u}) + \rho \boldsymbol{g} \tag{4}$$

The density ρ and the viscosity η are constants in this set of equations. The pressure p and the velocity $\boldsymbol{u}$ are the only state variables. Hence, $\boldsymbol{g}$ stands for the gravity.

3.2 RANS – Reynolds averaged Navier-Stokes equations

To describe turbulent flows, the *RANS* method is often used and it is also applied in this study. In this model the flow properties (ϕ) are decomposed according to the *Reynolds*-decomposing [9]. This means that the flow properties fluctuate in time t and space $\boldsymbol{x}$. They are split in the mean value ($\bar{\phi}$) and a fluctuating part (ϕ').

$$\phi(\boldsymbol{x}, t) = \bar{\phi}(\boldsymbol{x}) + \phi'(\boldsymbol{x}, t) \tag{5}$$

The mean value is calculated over a long period of time. [9]

$$\bar{\phi}(\boldsymbol{x}) = \lim_{\Delta t \to \infty} \frac{1}{\Delta t} \int_{t_0}^{t_0 + \Delta t} \phi(\boldsymbol{x}, t) \, dt \tag{6}$$

If the *RANS* method is applied to the pressure and velocity in formulas (3) / (4) and additional calculations are made, the mean continuum and the mean *Navier-Stokes* equations can be derived. [9]

$$\boldsymbol{\nabla} \cdot \bar{\boldsymbol{u}} = 0 \tag{7}$$

$$\rho \boldsymbol{\nabla} \cdot (\bar{\boldsymbol{u}}\bar{\boldsymbol{u}} + \overline{\boldsymbol{u}'\boldsymbol{u}'}) = -\boldsymbol{\nabla}\bar{p} + \eta \boldsymbol{\nabla} \cdot \boldsymbol{\nabla}[\boldsymbol{\nabla}\bar{\boldsymbol{u}} + (\boldsymbol{\nabla}\bar{\boldsymbol{u}})^{\boldsymbol{T}}] \tag{8}$$

Attention should be paid to formula (11) on the *Reynolds*-stresses $\underline{\tau}^{RS} = -\overline{\boldsymbol{u}'\boldsymbol{u}'}$. This term is unknown. As a result, the set of equations is not solvable. In order to solve these formulas, a turbulence model is required.

3.3 k-ω SST Model

One possibility to get an expression for the *Reynolds*-stresses is the application of "vortex viscosity models". In these methods the *Reynolds*-stresses get approximated with the turbulent viscosity and the turbulent kinetic energy. [10]

The *k-ω SST* (shear stress transport) model combines the *k-ε* and the *k-ω* models. For simple flows the *k-ε* model can be used. For example, this is the case inwards of flow fields, but next to a wall, whereby flows detach, it fails. In contrast to this the *k-ω* model is stable at walls but is less accurate inwards of flow fields. The *k-ω SST* is a combination of these two models: Next to walls the *k-ω* and in inner flow fields the *k-ε* model is used. In addition to that a mechanism is implemented, that limits the shear stress when the pressure is rising. [10]

In this study the *k-ω SST* model was used to solve the corresponding equations.

Turbulence frequency [10]

$$\omega = \frac{\varepsilon}{k} \tag{9}$$

Whereby ε is the turbulence dissipation and k the turbulence kinetic energy.

Turbulence viscosity η_t [10]

$$\eta_t = \frac{\rho a_1 k}{\max\left(a\omega, \sqrt{2S_{ij}S_{ij}F_2}\right)} \tag{10}$$

$$F_2 = \tanh\left({\phi_2}^2 \right) \tag{11}$$

$$\phi_2 = \max\left(\frac{2\sqrt{k}}{0{,}09\omega d_n}, \frac{500\eta}{\rho\omega {d_n}^2}\right) \tag{12}$$

$$S_{ij} = \frac{1}{2}\left(\frac{\partial u_i}{\partial j} + \frac{\partial u_j}{\partial i}\right) \tag{13}$$

(The equations are valid for a cartesian coordinate system with $i = x, y, z$ and $j = x, y, z$.)

The turbulence frequency and the turbulence kinetic energy are described with two transport equations. These can be found in literature e.g.: [10]. d_n describes the distance to the wall.

3.4 Flow Simulation

For the simulation of the following flows the solver *simpleFoam* [11] is used. This solver is a steady state solver for incompressible and turbulent flows. The corresponding equations can be found in [11].

OpenFOAM uses the *SIMPLE* algorithm to solve these equations. [12]

3.5 Particle Tracking

For the particle tracking a *Euler-Lagrangian* approach is used: the *MPPIC* (Multiphase particle in cell method). This means the particles are treated separately but the effect of the volume fraction of particles on the continuous phase is considered as well. [13].

3.5.1 Particle Equations

The most important equation for the particle tracking is the formula, which describes the evolution of the particle phase.

This equation is a *Liouville* equation for the particle distribution function $f(\boldsymbol{x}, \boldsymbol{u}, m, t)$, whereby $\boldsymbol{x}$ stands for the particle position, $\boldsymbol{u}$ for the particle velocity, m for the particle mass and t for time. [14]

$$\frac{\partial f}{\partial t} + \boldsymbol{\nabla} \cdot (f\boldsymbol{u}) + \boldsymbol{\nabla}_{\boldsymbol{u}} \cdot (f\boldsymbol{A}) = 0 \tag{14}$$

A describes the particle acceleration with $\boldsymbol{u_G}$ the velocity of the gas, ρ_s the particle density, θ the particle-phase volume fraction, the inter-particle stress τ and the drag coefficient D.

$$\boldsymbol{A} = D(\boldsymbol{u_G} - \boldsymbol{u}) - \frac{1}{\rho_s}\nabla p + \boldsymbol{g} - \frac{1}{\theta\rho_s}\boldsymbol{\nabla}\tau \tag{15}$$

The formula consists of four parts. The first term represents the drag force, then there is the pressure gradient, followed by gravity $\boldsymbol{g}$ and at the end is the influence of the inter-particle stress. [15]

The mass and momentum equation of the gas phase can be found in [14].

3.5.2 Drag

The drag forces are computed based on the *Gidaspow* drag model, which is a combination of the *Wen-Yu* and *Ergun* drag models. [16] In these equations F_D represents the drag forces, C_D the particle drag coefficient, Re_p the particle *Reynolds* number, d_p the particle diameter, u_{rel} the relative velocity between the particle and the carrier, α_c the volume fraction of the carrier fluid and ρ_c / μ_c the density / dynamic viscosity of the carrier at the cell, where the particle is positioned.

$$F_{D,Wen-Yu} = \frac{3}{4}\frac{(1-\alpha_c)\mu_c\alpha_c Re_p}{d_p^2}C_D\alpha_c^{-2,65} \tag{16}$$

$$F_{D,Ergun} = \left(150\frac{1-\alpha_c}{\alpha_c} + 1,75Re_p\right)\frac{(1-\alpha_c)\mu_c}{d_p^2} \tag{17}$$

$$Re_p = \frac{\rho_c|u_{rel}|d_p}{\mu_c} \tag{18}$$

$$F_D = F_{D,Wen-Yu} \qquad \alpha_c \geq 0,8 \tag{19}$$

$$F_D = F_{D,Ergun} \qquad \alpha_c < 0,8 \tag{20}$$

Drag coefficient used by Gidaspow [17]

$$C_D = \frac{24}{\alpha_c Re_p}\left[1 + 0,15(\alpha_c Re_p)^{0,687}\right] \qquad \alpha_c Re_p < 1000 \tag{21}$$

$$C_D = 0{,}44 \qquad\qquad \alpha_c Re_p > 1000 \tag{22}$$

3.5.3 Particle Stress

The inner-particle stress is based on the *Harris* and *Crighton* stress model [15]. This formula consists of four constants and is only a function of the particle volume fraction θ.

$$\boldsymbol{\nabla}\tau = \frac{P_S\theta^{\beta}}{\max\left[(\theta_{CP}-\theta),\varepsilon(1-\theta)\right]} \tag{23}$$

In this model P_S stands for the particle pressure, θ_{CP} for the maximum volume fraction and β / ε respectively are model constants.

4. General Simulation Setup

To get an understanding of the fluid mechanical conditions in the nasal interiors, *CFD* simulations are necessary. In this chapter the general simulation setup for the flow - and particle simulations with *OpenFOAM* is discussed. In particular, the generation of the mesh is presented. The aim of this study is to create particle tracking simulations with two different nasal geometries and analyse the data which is obtained.

4.1 Geometry

In this study two nasal airways are observed. The geometries for the first test object (A) were provided as ready to use stereolithography files. In figure 8 the two *STL* files are shown: The upper nasal airways and a sphere, which is used for the boundary conditions.

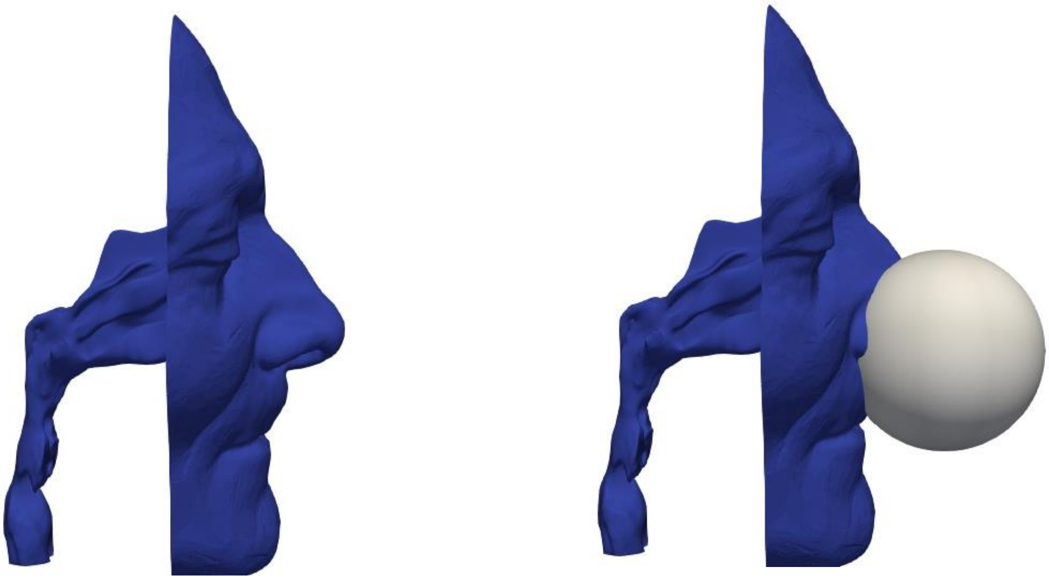

Figure 8: Test object A: Left – upper nasal airways, right – upper nasal airways with sphere

In contrast to this, for the second test object (B), only the raw data of the scans were provided (figure 9).

With the use of the program *MeshLab* the relevant part of the scan was exposed (figure 10). Following this the geometry was cleaned with the software *Blender*. This means sharp edges were removed and the whole object was smoothed. In the end the geometry was locally smoothed with the program *Meshmixer* (figure 10).

For the simulations, two *STL* files are needed. The first one consists of the nasal airways, which should be investigated and the second one is a sphere, which is put over the nose to set suitable boundary conditions. The sphere is hollow and has an opening, where the tip of the nose fits right in. The hollow ball for test object A was provided and for test object B it was made with the software *Inventor* and edited with *Blender* to receive a ball, which fits exactly over the nose. In the end the *STL* files for test object B are scaled to have the right scale in *OpenFOAM* (figure 11).

TU Bibliothek, WIEN Your knowledge hub
Die approbierte gedruckte Originalversion dieser Diplomarbeit ist an der TU Wien Bibliothek verfügbar
The approved original version of this thesis is available in print at TU Wien Bibliothek.

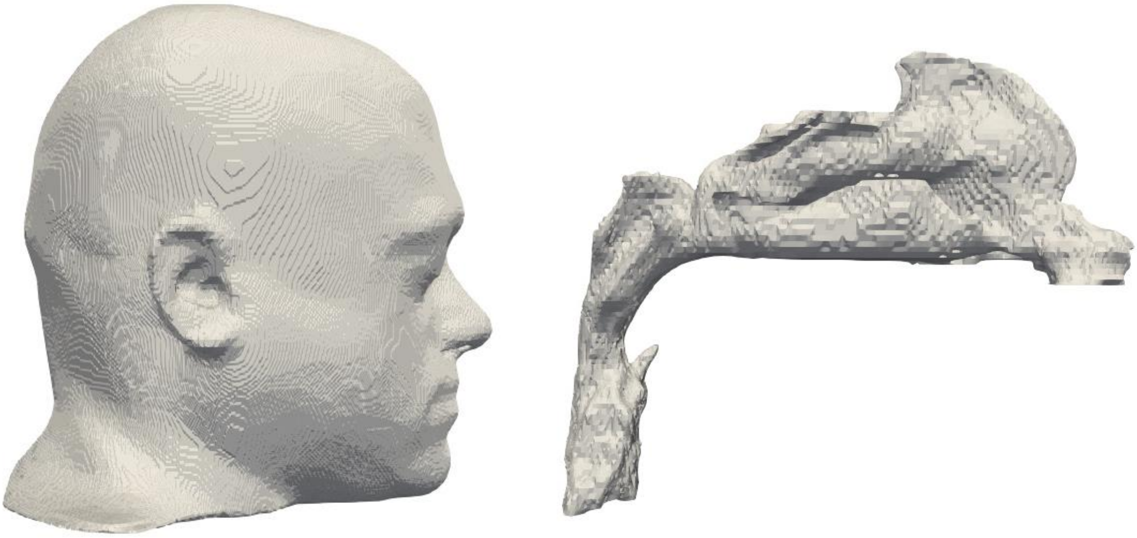

Figure 9: Test object B: Left – head with upper nasal airways, right – corresponding negative image

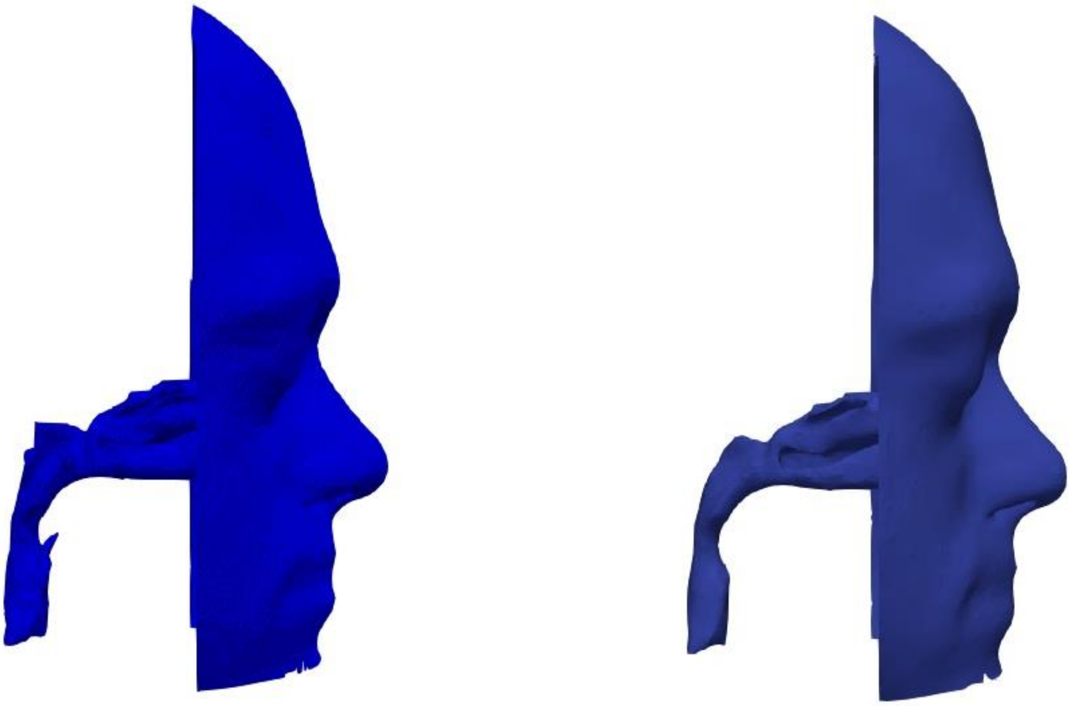

Figure 10: Test object B: Left – relevant geometry, right – geometry after cleaning, general and local smoothing

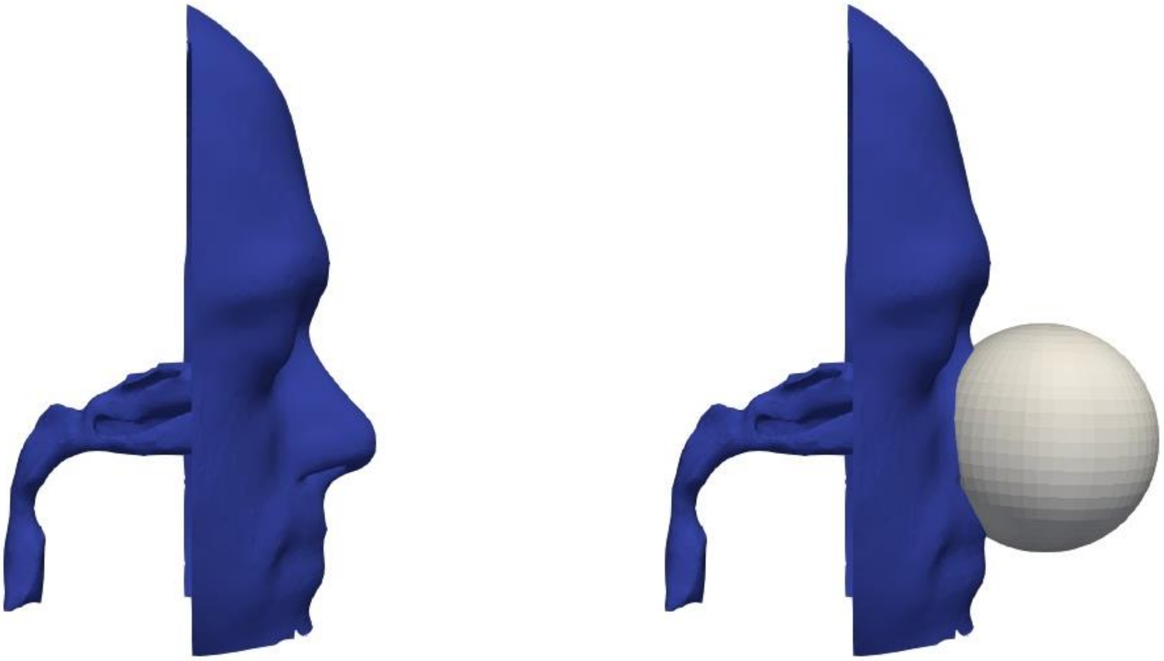

Figure 11: Test object B: Left – upper nasal airways, right – upper nasal airways with sphere

4.2 Mesh Generation

To produce a robust simulation a proper mesh is essential. For detailed explanations of the mesh generation refer to [18].

In general, a suitable geometry is needed. As already described in the previous chapter, two *STL* files are required for the simulations. In the following description of the process to receive a suitable mesh, the geometry of test object A is used (figure 8).

4.2.1 BlockMesh

At first a background mesh has to be created. This can be done by the command *blockMesh*. To get a fine mesh in the whole domain, the number of cells in the *BlockMeshDict* can be raised.

4.2.2 SnappyHexMesh

After this step the command *SnappyHexMesh* can be executed.

This command is necessary to create a suitable mesh out of *STL* files, which can be used to investigate simulations with complex geometries.

The settings for this command are located in the *SnappyHexMeshDict*. It starts with a cell splitting process (figure 12), according to the edges, which are stored in the *edgeMesh* file. This file is produced by the command *surfaceFeatures* and all edges are selected, according to the *SurfaceFeaturesDict*. In the *SnappyHexMeshDict* the refinement level for the surfaces can be selected.

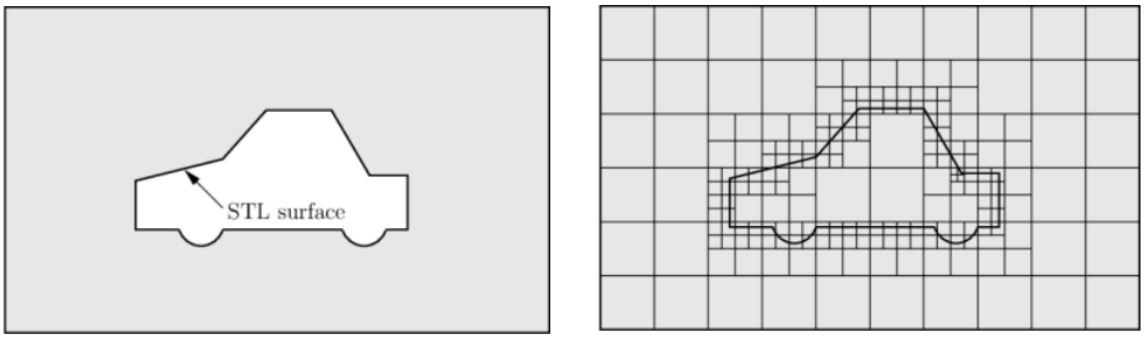

Figure 12: SnappyHexMesh; Left - STL surface, Right - cell splitting and background mesh [18]

After the cell splitting process, the cell removal starts (figure 13). To specify which cells should be removed, a point in the domain which shall remain, is selected. For this step, a closed area is needed. In the case of the flow in the nasal interiors, a point is selected, so that the nasal airways remain.

Cells, which lay in both domains, stay if more than about 50% of their volume lay in the region, which retains. [18]

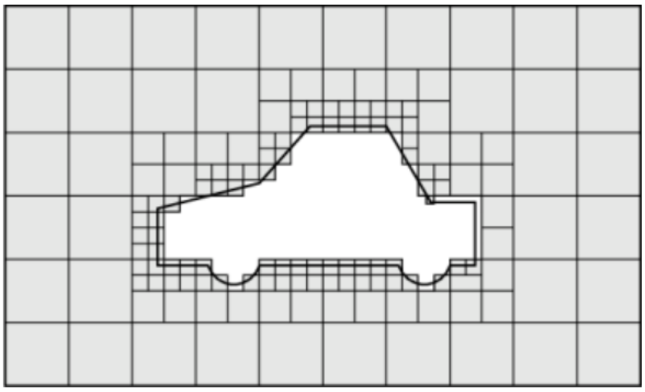

Figure 13: SnappyHexMesh; Cell removal process [18]

In the case a specific region has to be refined, extra refinement regions can be defined in the *SnappyHexMeshDict*. In the present simulations, no extra refinement regions are selected.

After the cells were successfully refined and removed the snapping process takes place. A detailed description of this process can be found in [18]. The aim of this step is to smooth the jagged contour of the domain and raise the quality of mesh resulting from a *STL* file (figure 14).

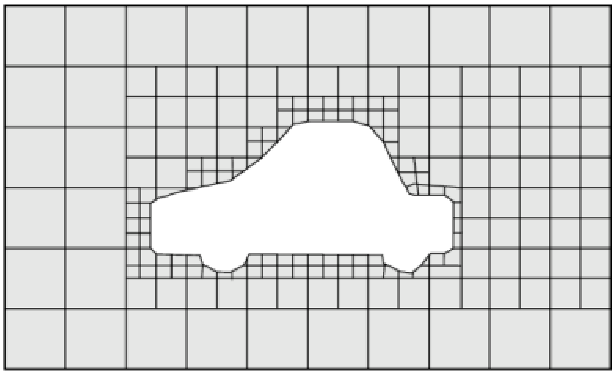

Figure 14: SnappyHexMesh; Snapping process [18]

The S*nappyHexMesh* method also provides a feature to create mesh layers, but this function is not used for the present nasal simulations.

4.2.3 Mesh

The produced mesh of test object A (figure 15) contains 5 879 104 cells and of test object B (figure 17) contains 2 778 021 cells. In figure 16 a zoom of the region before the outlet of test object A is presented.

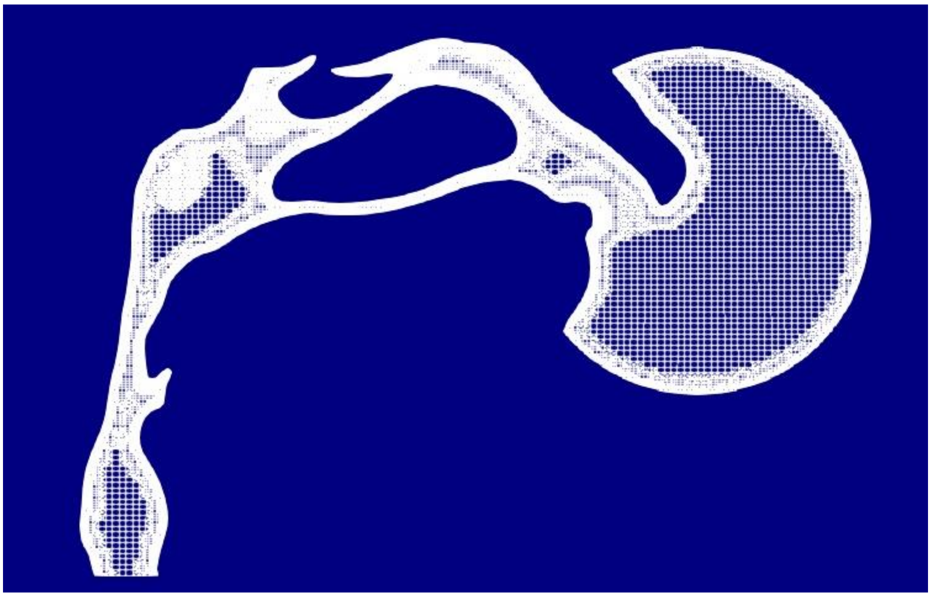

Figure 15: Main slice of the mesh – test object A

Die approbierte gedruckte Originalversion dieser Diplomarbeit ist an der TU Wien Bibliothek verfügbar
The approved original version of this thesis is available in print at TU Wien Bibliothek.
TU WIEN Bibliothek Your knowledge hub

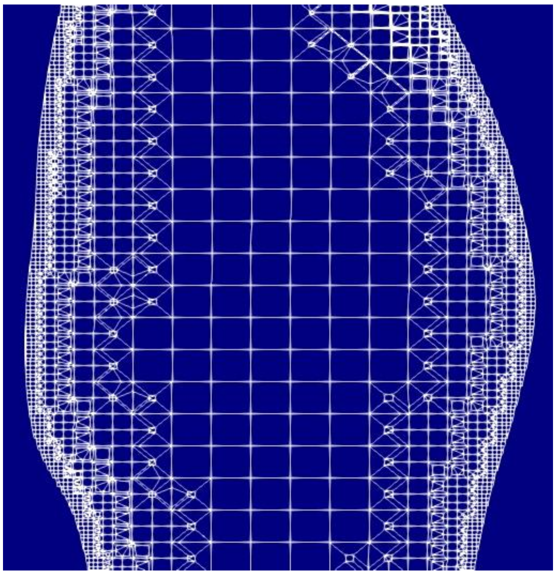

Figure 16: Mesh detail – outlet – test object A

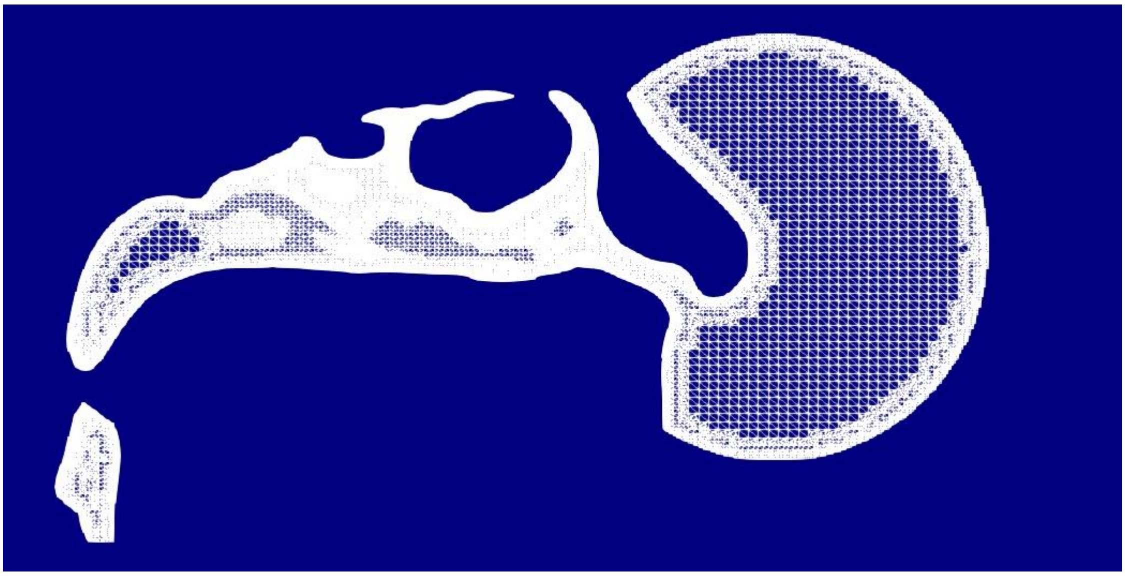

Figure 17: Main slice of the mesh – test object B

5. Flow Simulation

After the mesh was created, the setup for the flow simulation can be made. As described before, a flow simulation has to be conducted and based on the achieved results, a particle tracking is executed.

5.1 Setup

To start the simulation, proper boundary conditions have to be set. In the present case three regions are defined, which can be used for this task. In figure 18 and figure 19 the three domains for the two test objects are presented. The inlet and the wall are based on the *STL* files, which are called for test object A *clownose*/*testa* and for test object B *noseball6/face_cut6*. The patches for the outlet are assigned to *defaultFaces*, because they do not correspond to any of the *STL* files.

Die approbierte gedruckte Originalversion dieser Diplomarbeit ist an der TU Wien Bibliothek verfügbar
The approved original version of this thesis is available in print at TU Wien Bibliothek.
TU WIEN Bibliothek Your knowledge hub

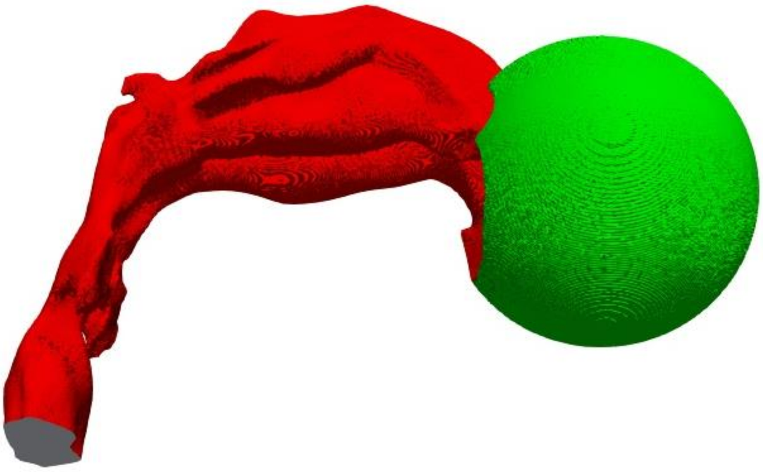

Figure 18: Test object A – regions: Grey - outlet, red – wall, green – inlet

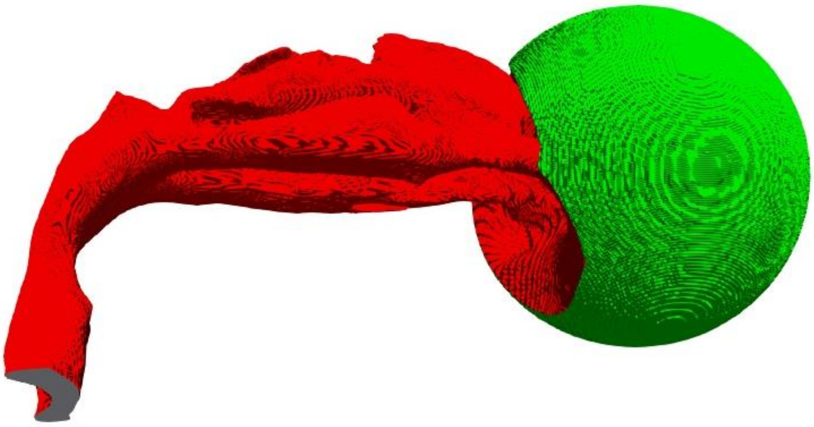

Figure 19: Test object B – regions: Grey – outlet, red – wall; green – inlet

At the inlet a volumetric flow is injected and streams through the nasal airways to the outlet. The pressure and velocity conditions are set regarding the following code (code of test object A). (The value of the flowrate was changed to obtain different simulation results.)

```
    object      p;
}
// * * * * * * * * * * * * * * * * * * * * * * * * * * * * * * * * * * * * * //

dimensions      [0 2 -2 0 0 0 0];

internalField   uniform 0;

boundaryField
{
    defaultFaces
    {
        type            fixedValue;
        value           uniform 0;
    }
    testa
    {
        type            zeroGradient;
    }
    clownose
    {
        type            zeroGradient;
    }
}

// ************************************************************************* //
```

```
    object      U;
}
// * * * * * * * * * * * * * * * * * * * * * * * * * * * * * * * * * * * * * //

dimensions      [0 1 -1 0 0 0 0];

internalField   uniform (0 0 0);
```

```
boundaryField
{
    clownose
    {
        type                  flowRateInletVelocity;
        volumetricFlowRate    constant 0.0008;
    }

    defaultFaces
    {
        type            pressureInletOutletVelocity;
        value           uniform (0 0 0);
    }

    testa
    {
        type            fixedValue;
        value           uniform (0 0 0);
    }
}

// ************************************************************************* //
```

The solver *simpleFoam* is used in the present study. This solver is a steady state solver for incompressible and turbulence flow. [19]

5.2 Results

In the following chapters the velocity fields of the two upper nasal airways are presented and described. Further analyses are done in chapter “7. Analysis”.

5.2.1 Test object A

In figure 20 to figure 23 the steady state of the velocity for an inlet flowrate of 5 l/min is pictured. The magnitude increases in the vertical throat after the nasal cavity. This result makes sense regarding the cross-sectional area (figure 5), the area decreases after the nasal cavity. Thus, the velocity increases.

The component in the Y-direction is shown in figure 22. The region with the highest horizontal velocity is in the nasal cavity. Moreover figure 23 illustrates that the domains, with the highest velocity values in Z-direction are behind the nostrils and in the throat. Hence more or less the flow starts vertically, then changes rapidly into a horizontal stream and then again modifies to a vertical flow.

In the end the velocity in X-direction is negligible.

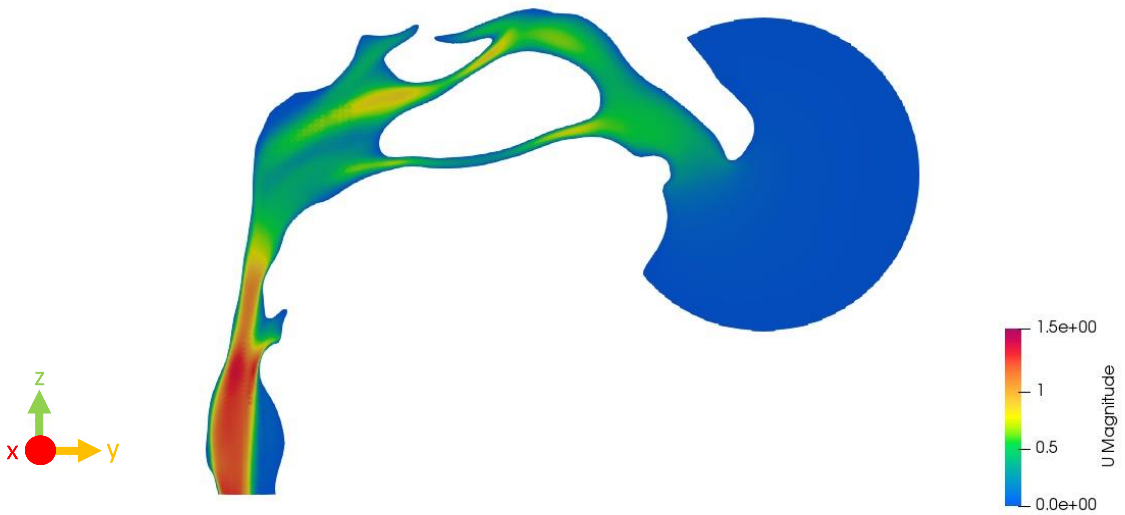

Figure 20: Velocity magnitude in m/s – 5 l/min – test object A

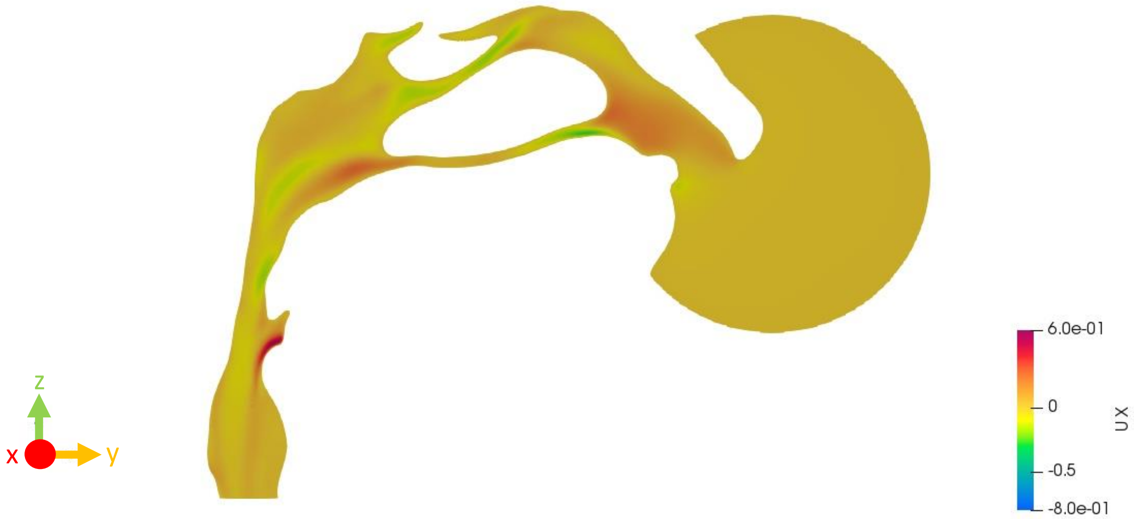

Figure 21: Velocity X-component in m/s – 5 l/min – test object A

Die approbierte gedruckte Originalversion dieser Diplomarbeit ist an der TU Wien Bibliothek verfügbar
The approved original version of this thesis is available in print at TU Wien Bibliothek.
TU WIEN Bibliothek Your knowledge hub

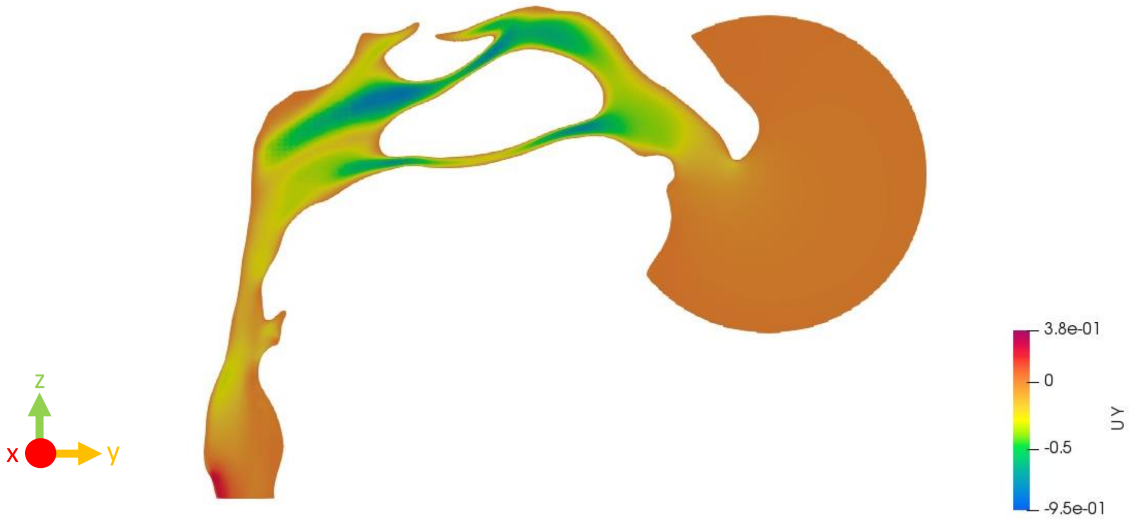

Figure 22: Velocity Y-component in m/s – 5 l/min – test object A

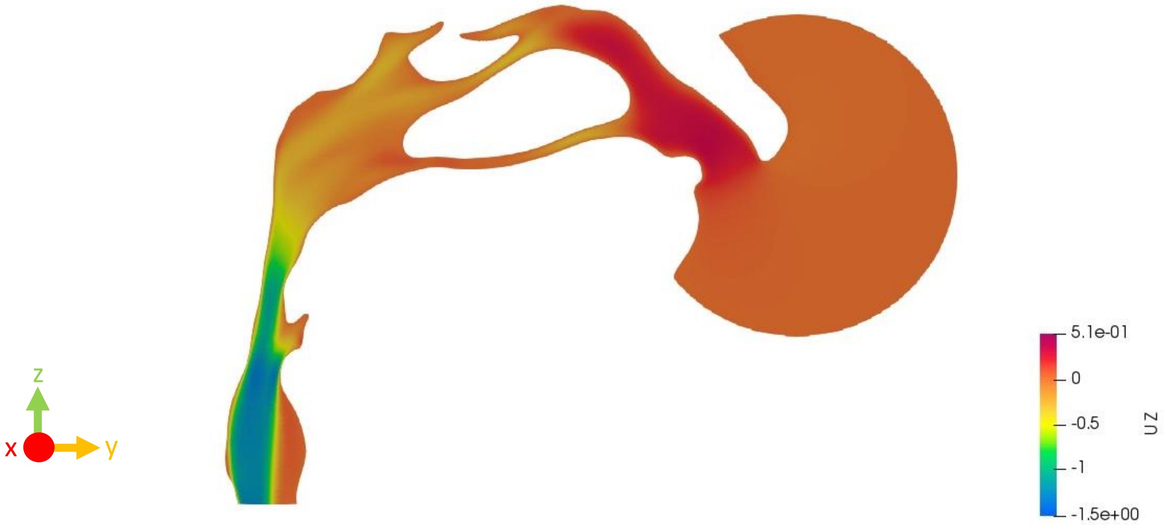

Figure 23: Velocity Z-component in m/s – 5 l/min – test object A

The goal of this study is to investigate particle tracking for different flowrates. For test object A four different flowrates are applied: 5 l/min (figure 20), 10 l/min (figure 24), 15 l/min (figure 25), 20 l/min (figure 26). The figures show clearly that the different steady state solutions are similar to each other.

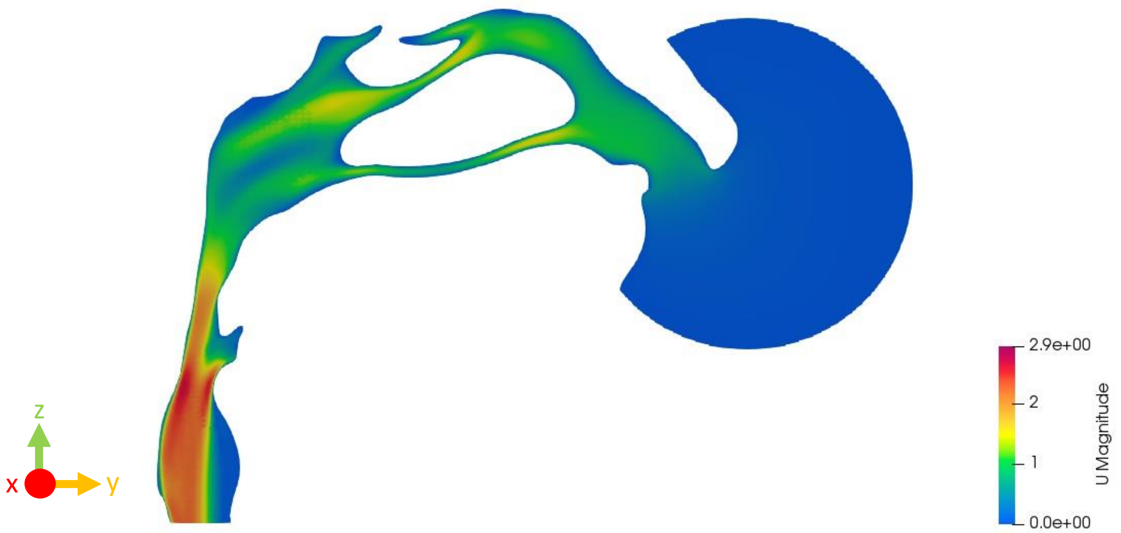

Figure 24: Velocity magnitude – 10 l/min – test object A

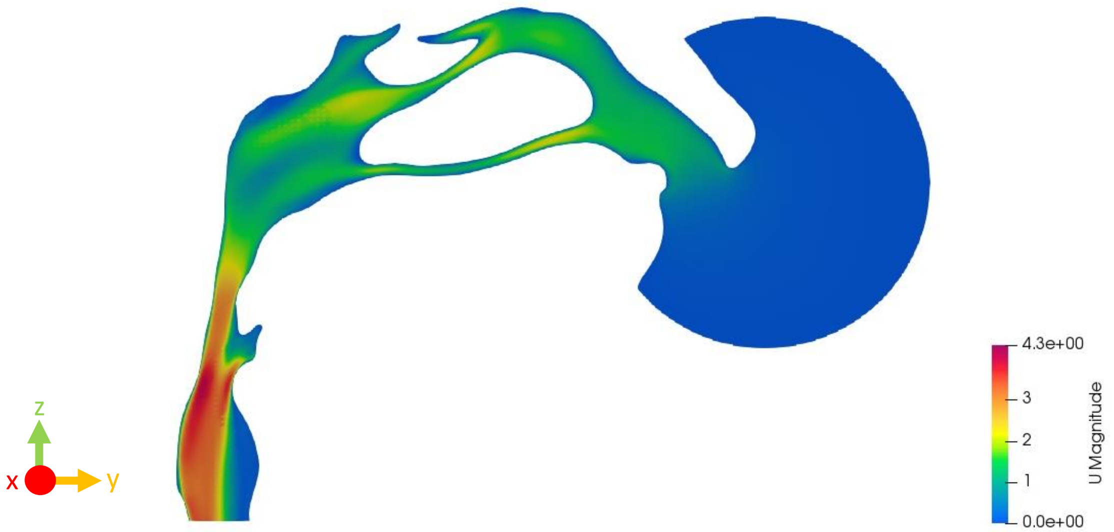

Figure 25: Velocity magnitude – 15 l/min – test object A

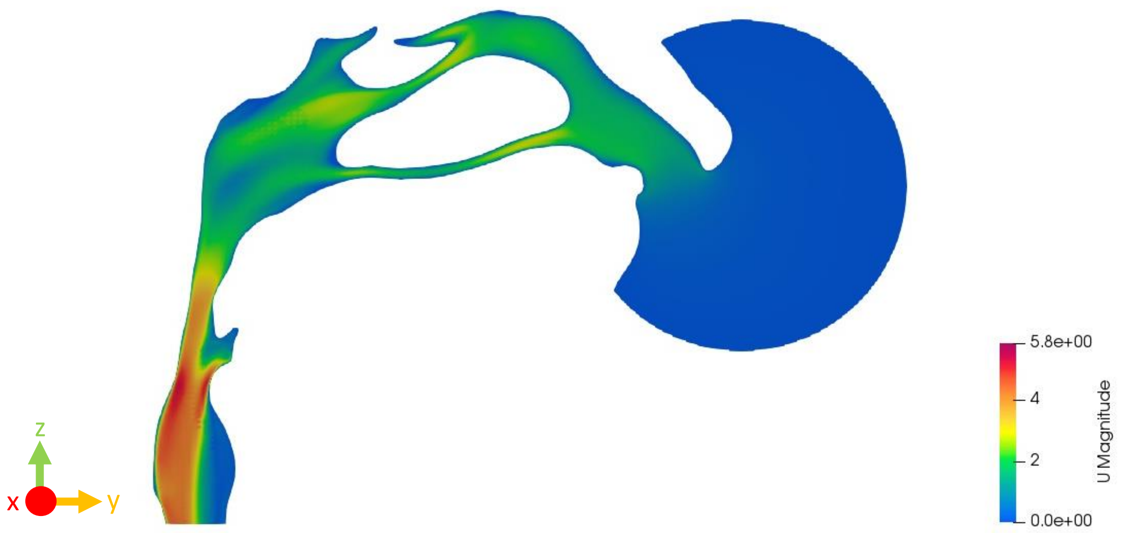

Figure 26: Velocity magnitude – 20 l/min – test object A

5.2.2 Test object B

The flow characteristics of test object B were investigated applying six different flowrates (5 l/min, 10 l/min, 15 l/min, 20 l/min, 60 l/min and 120 l/min). The velocity fields of the corresponding magnitudes and of different sections are presented in figure 27 to figure 40. It is clear to see (figure 27 to figure 36) that in sections with a small cross sectional area, for example in the region of the throat and the nostrils, the magnitude has the highest values. Moreover figure 37 to figure 40 clearly show that the relevant flow field exists only in a central area. As shown in the results of test object A, the different steady state solutions of test object B are similar to each other.

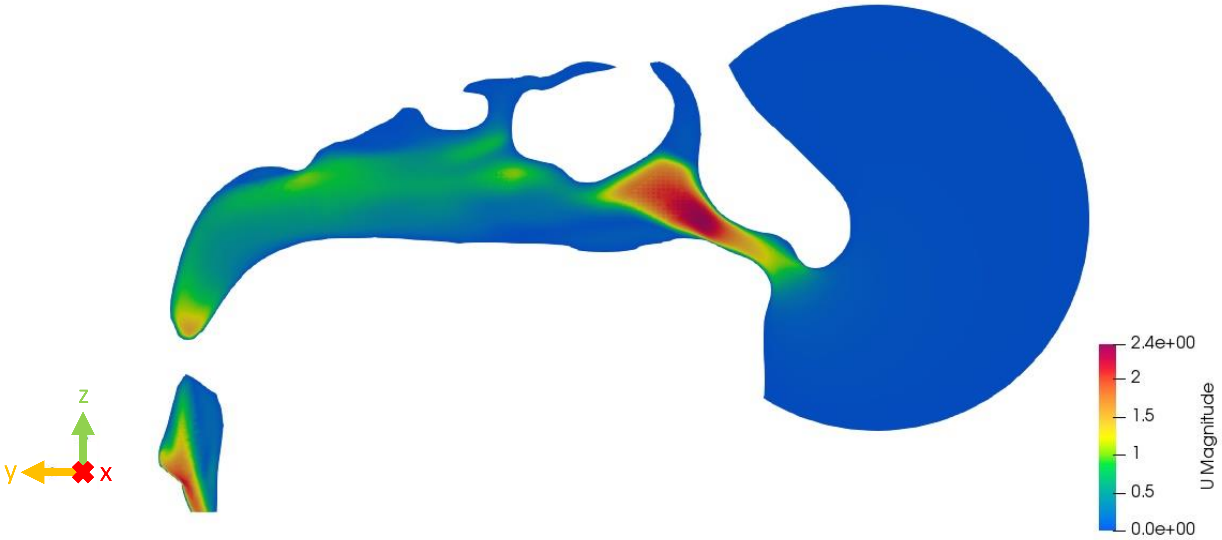

Figure 27: Velocity magnitude – 5 l/min – test object B – main section

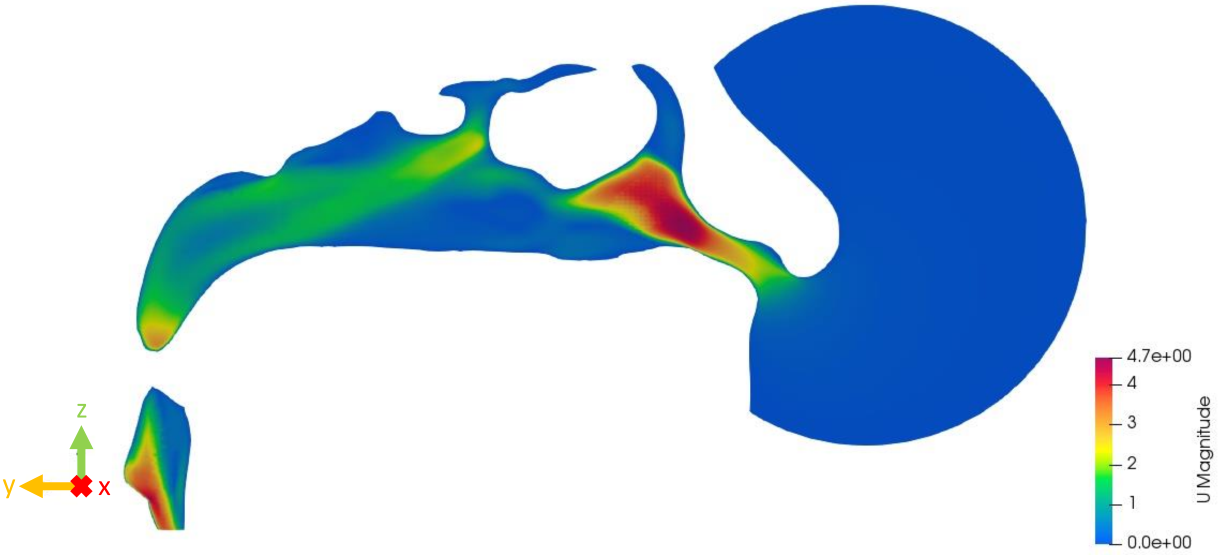

Figure 28: Velocity magnitude – 10 l/min – test object B – main section

Die approbierte gedruckte Originalversion dieser Diplomarbeit ist an der TU Wien Bibliothek verfügbar
The approved original version of this thesis is available in print at TU Wien Bibliothek.
TU WIEN Bibliothek Your knowledge hub

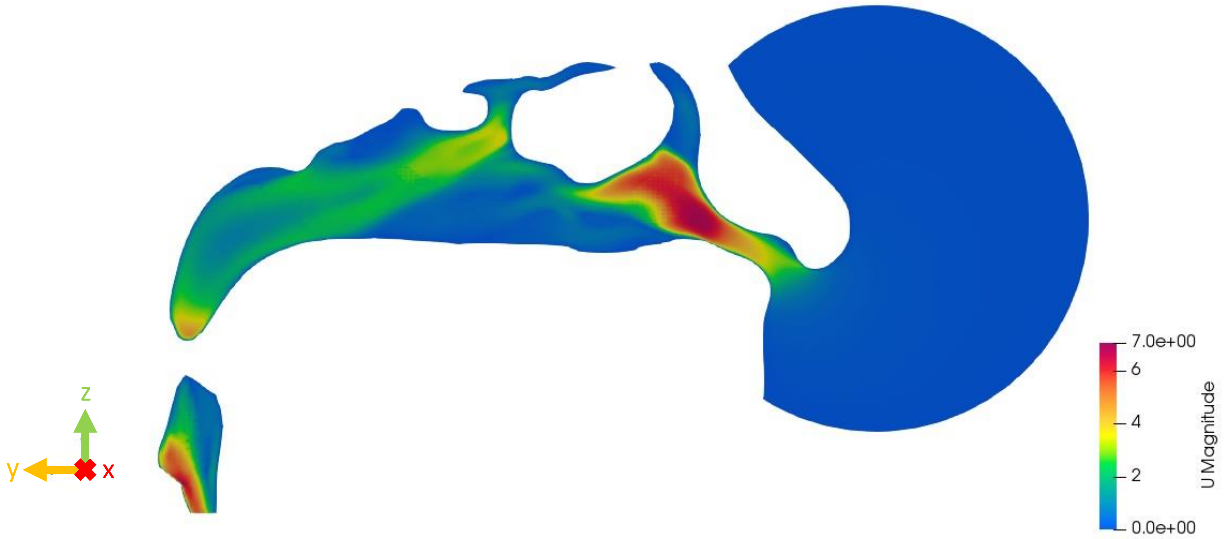

Figure 29: Velocity magnitude – 15 l/min – test object B – main section

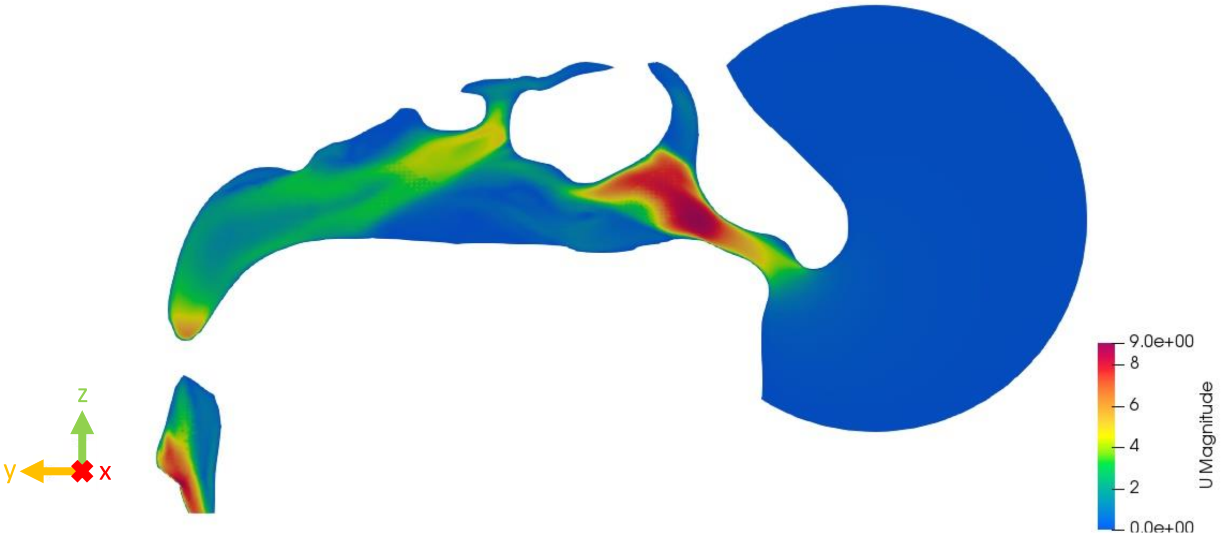

Figure 30: Velocity magnitude – 20 l/min – test object B – main section

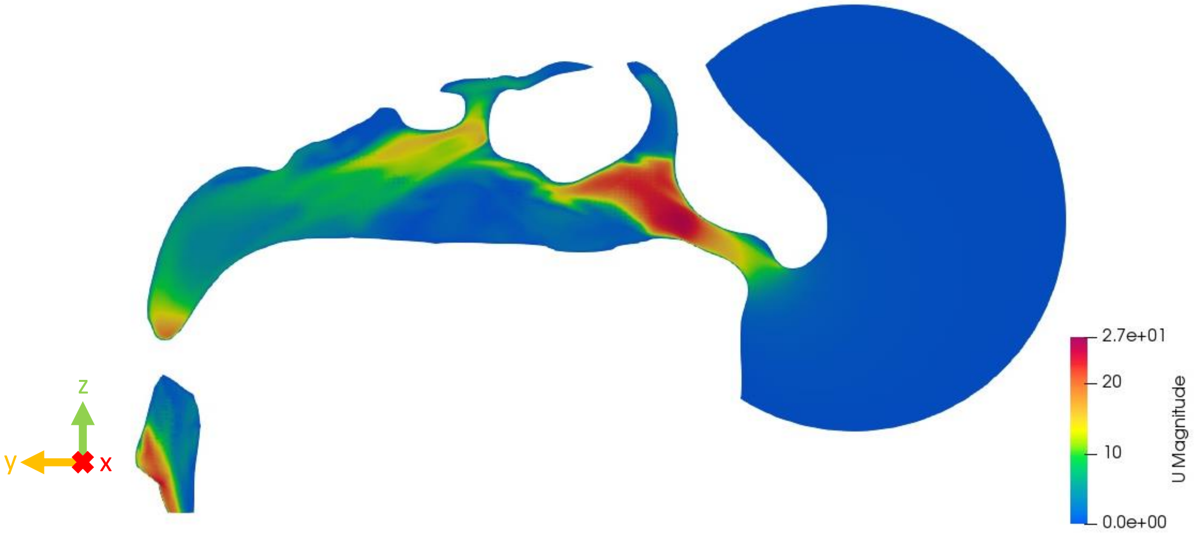

Figure 31: Velocity magnitude – 60 l/min – test object B – main section

Die approbierte gedruckte Originalversion dieser Diplomarbeit ist an der TU Wien Bibliothek verfügbar
The approved original version of this thesis is available in print at TU Wien Bibliothek.
TU Bibliothek Your knowledge hub WIEN

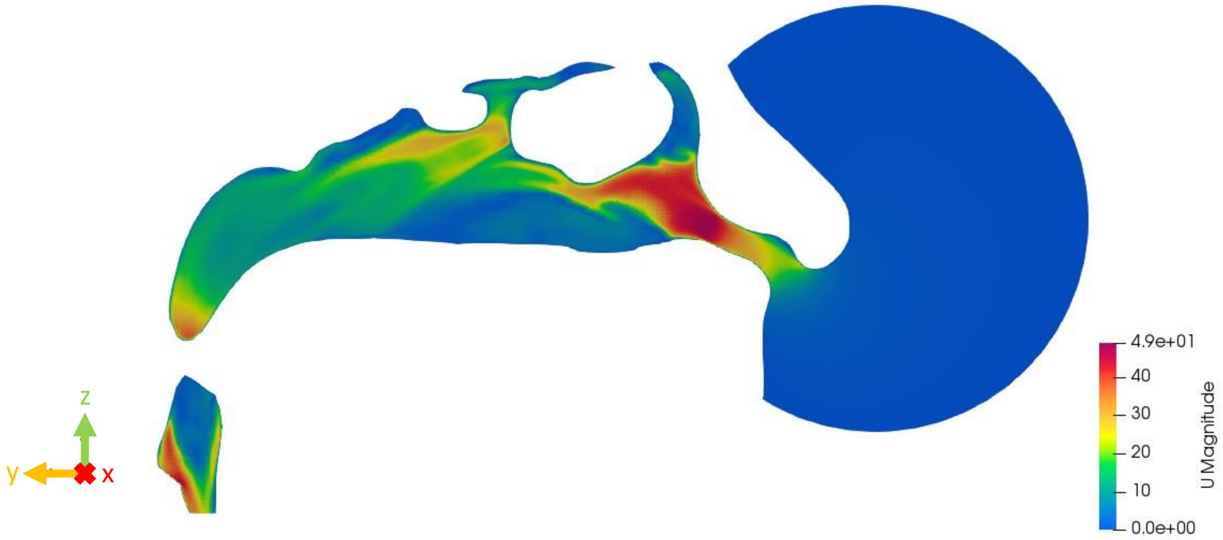

Figure 32: Velocity magnitude – 120 l/min – test object B – main section

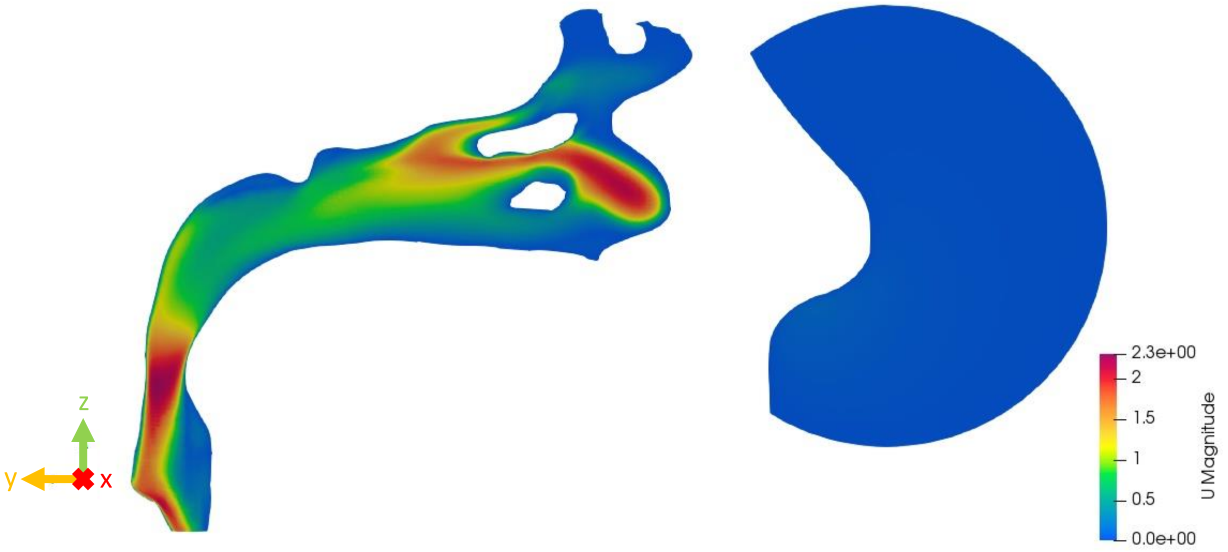

Figure 33: Velocity magnitude – 5 l/min – test object B – throat

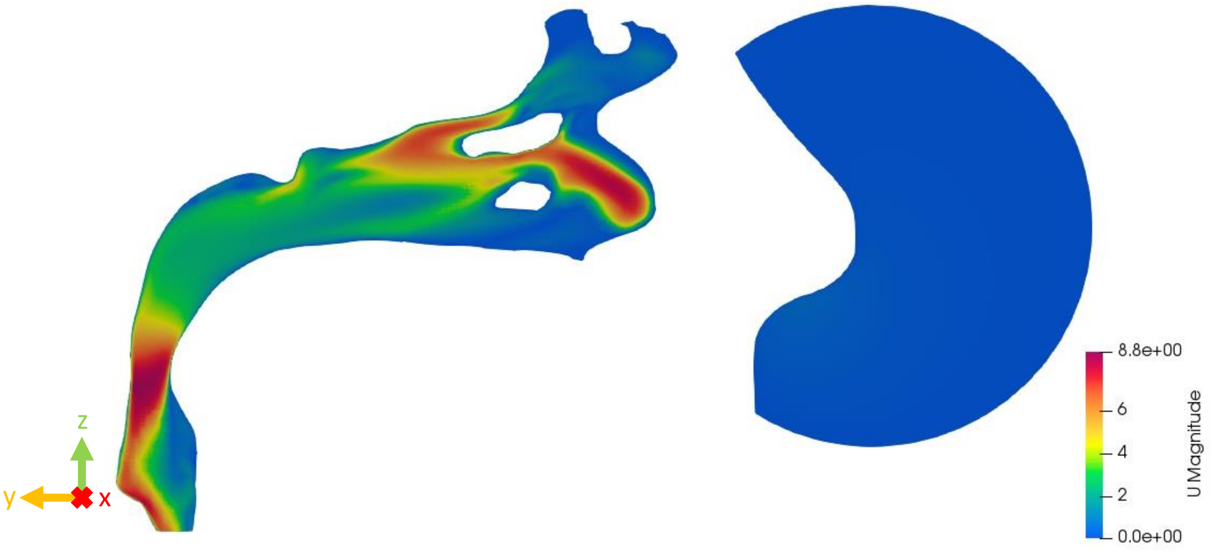

Figure 34: Velocity magnitude – 20 l/min – test object B – throat

Die approbierte gedruckte Originalversion dieser Diplomarbeit ist an der TU Wien Bibliothek verfügbar
The approved original version of this thesis is available in print at TU Wien Bibliothek.
TU WIEN Bibliothek Your knowledge hub

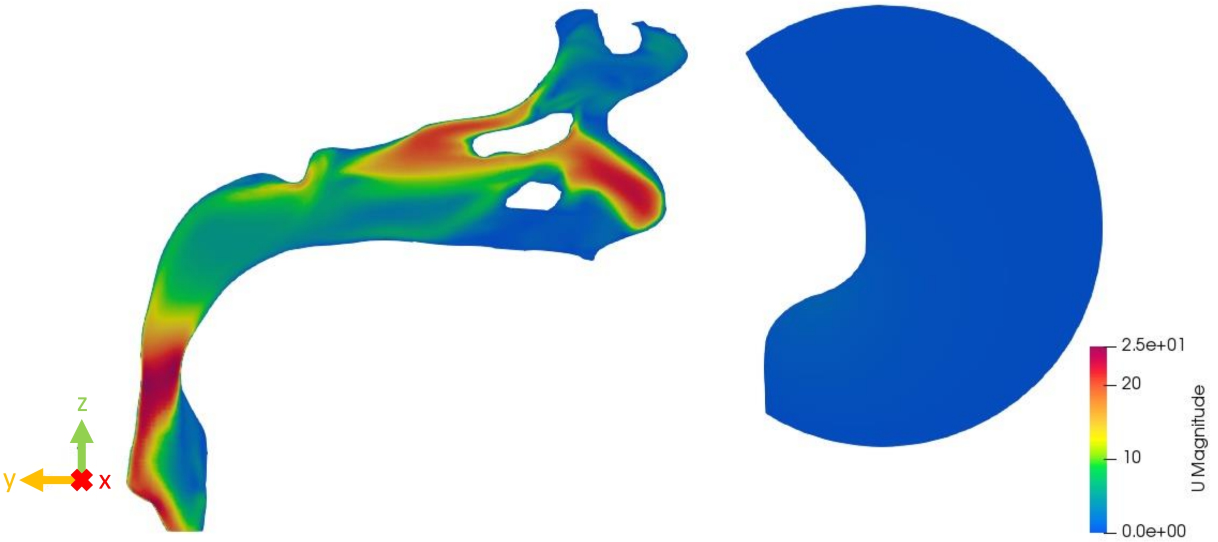

Figure 35: Velocity magnitude – 60 l/min – test object B – throat

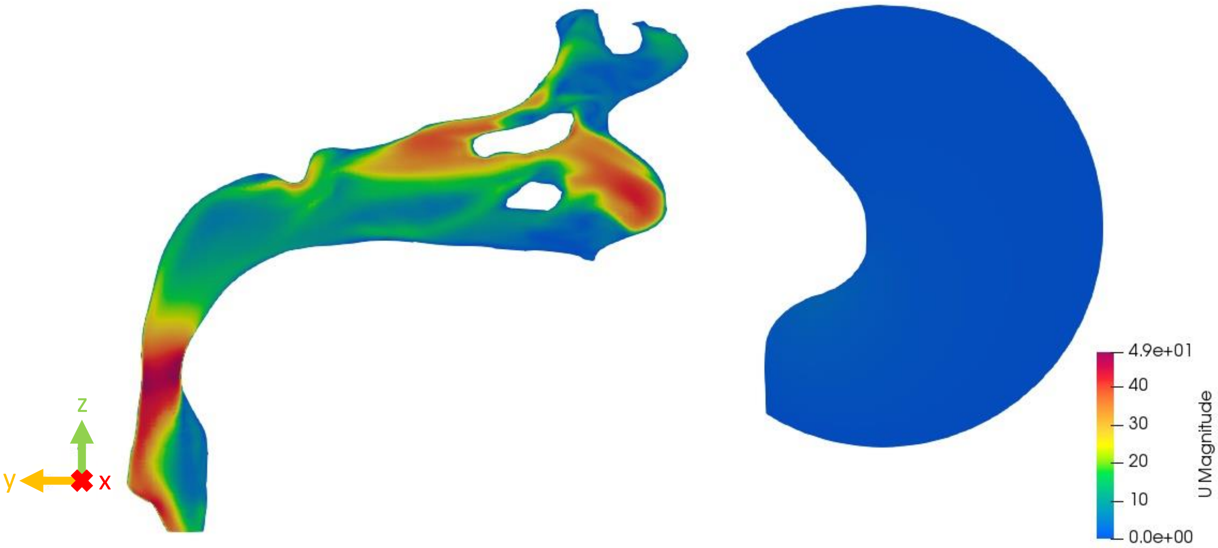

Figure 36: Velocity magnitude – 120 l/min – test object B – throat

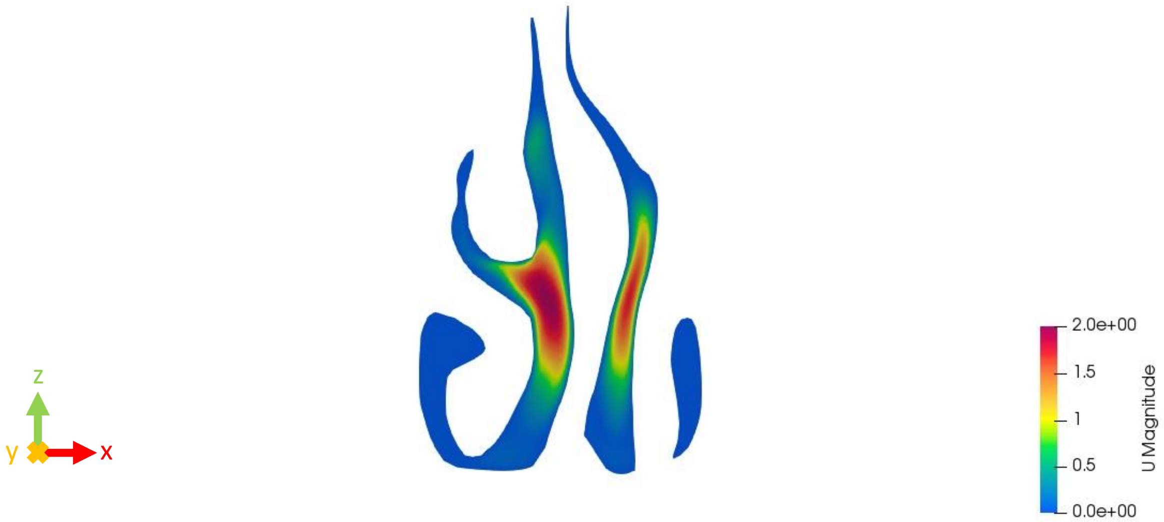

Figure 37: Velocity magnitude – 5 l/min – test object B – turbinates

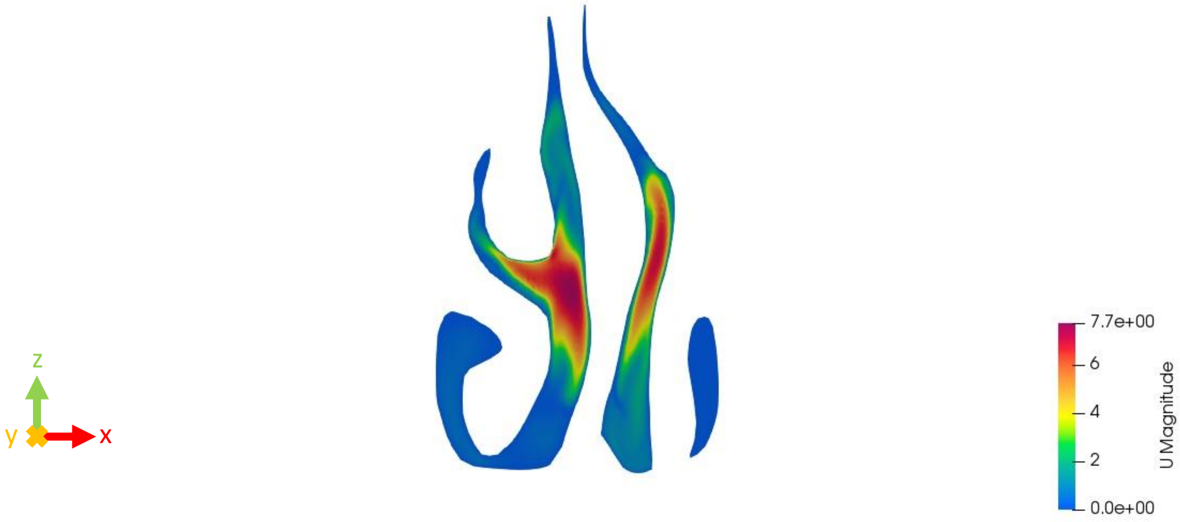

Figure 38: Velocity magnitude – 20 l/min – test object B – turbinates

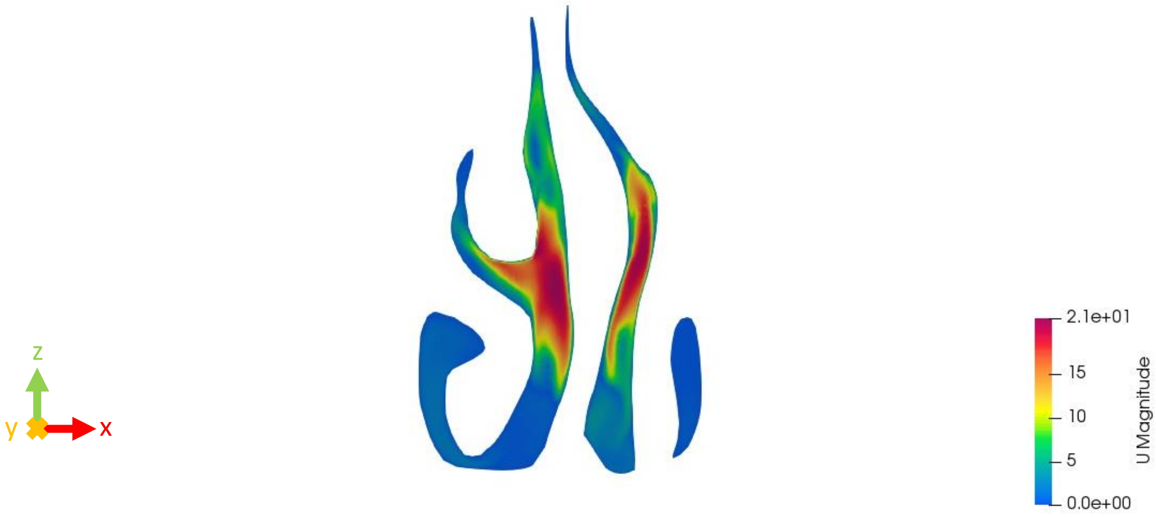

Figure 39: Velocity magnitude – 60 l/min – test object B – turbinates

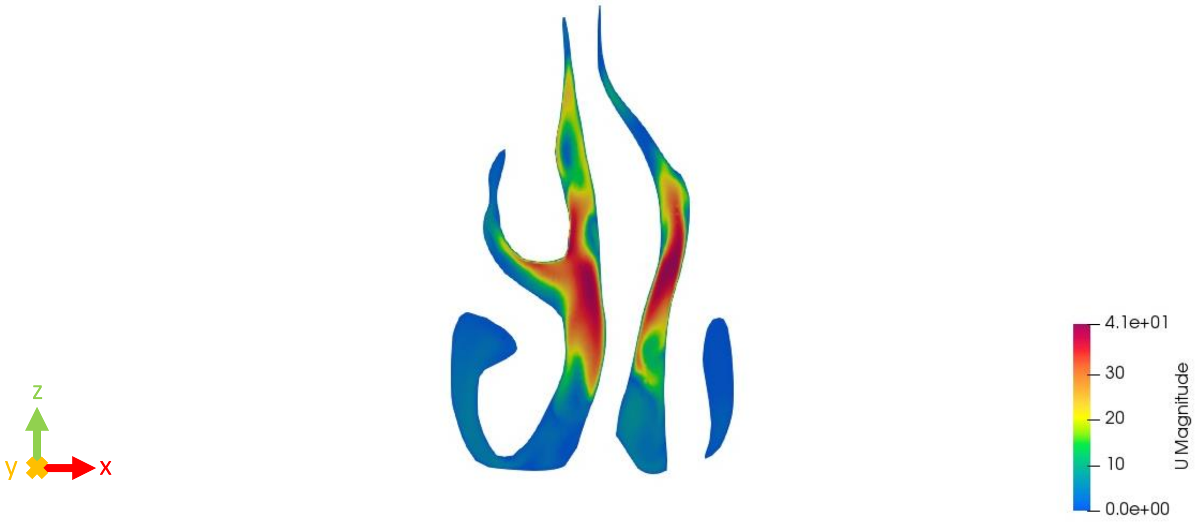

Figure 40: Velocity magnitude – 60 l/min – test object B – turbinates

6. Particle Tracking Simulation

There are many possibilities to produce a particle tracking with *OpenFOAM*. In this study, particle trackings based on steady state solutions (see chapter 5. Flow Simulation) were produced.

6.1 Setup

The command *denseParticleFoam* is used to start the particle simulation. The main dictionary is called *cloudProperties*.

The density of the particles is set equal to the density of water.

```
{
    rho0            1000; //density of particles
}
```

The considered particle forces are the drag force based on the *Gidaspow* model [20] and the forces resulting cause of gravity: The gravity force and the buoyancy force.

```
{
    particleForces
    {
        ErgunWenYuDrag
        {
            alphac alpha.air;
        }
        gravity;
    }
```

The particles get injected at the sphere on the nose and the *SOI* is set to the last produced time step of the according flow simulation. This means that the injection starts one time step after the SOI and the duration of the injection is set to 1 s. The simulation time in the *controlDict* is set to 1 s as well and the time step is set to 0,005 s. So according to this information in sum 19900 particles are injected in one standard simulation. The particles start with 0 m/s and the size of the particles is fixed to one specific size. In this study two particle tracking models are observed. The first model with test object A got investigated with six particle sizes and four different flowrates (1 µm, 5 µm, 10 µm, 20 µm, 30 µm, 50 µm – 5 l/min, 10 l/min, 15 l/min, 20 l/min). In total 24 simulations are produced and analysed. In contrast to that with test object B six particle sizes and two different flowrates got combined (1 µm, 5 µm, 10 µm, 20 µm, 30 µm, 50 µm – 5 l/min, 20 l/min). Hence twelve simulations are carried out and furthermore, investigated.

```
injectionModels
{
   model1
    {

        type            patchInjection;
        massTotal       1.570796327e-10;//unnecessary by fixed value
        SOI             802;
        parcelBasisType fixed;
        patchName       clownose;
        duration        1;
        parcelsPerSecond 20000;
        nParticle 1;
        U0               (0 0 0);
        flowRateProfile constant 1;
        sizeDistribution
        {
            type        fixedValue;
            fixedValueDistribution
            {
                value 1e-6;

            }
        }
    }
}
```

To model the sticky surfaces of the nasal interiors the wall is equipped with a stick condition. This means particles that collide with the surfaces of the *testa* or *face_cut6* will stick and the velocity will be set to 0 m/s.

```
patchInteractionModel localInteraction;

 localInteractionCoeffs
 {
    patches
    (
         testa
        {
            type stick;

        }
        clownose
        {
            type rebound;
            e    1;
            mu   0;
        }
        defaultFaces
        {
            type escape;
        }
    );
}
```

In this study the inter-particle stress model of *Harris* and *Crighton* [21] is used. The constants can be seen in the following section.

```
implicitCoeffs
{
    alphaMin 0.0001;
    rhoMin 1.0;
    applyLimiting true;
    applyGravity false;
    particleStressModel
    {
        type HarrisCrighton;
        alphaPacked 0.6;
        pSolid 5.0;
        beta 2.0;
        eps 1.0e-2;
    }
}
```

Die approbierte gedruckte Originalversion dieser Diplomarbeit ist an der TU Wien Bibliothek verfügbar
The approved original version of this thesis is available in print at TU Wien Bibliothek.
TU WIEN Bibliothek Your knowledge hub

6.2 Results

All in all, 36 results are obtained. The analysis of these simulations can be found in chapter “7. Analysis”. In general, three main situations can occur. The first situation is a case, where nearly all particles which enter the corresponding geometry get carried away by the stream through the volume (figure 41 and figure 44). The other extreme situation occurs when nearly all particles which enter the corresponding geometry collide with the nasal walls and get stuck (figure 42 and figure 45). Between these two cases there is a mixed situation, where particles flow through the nasal interiors while other particles stick to the wall and deposit there (figure 43 and figure 46).

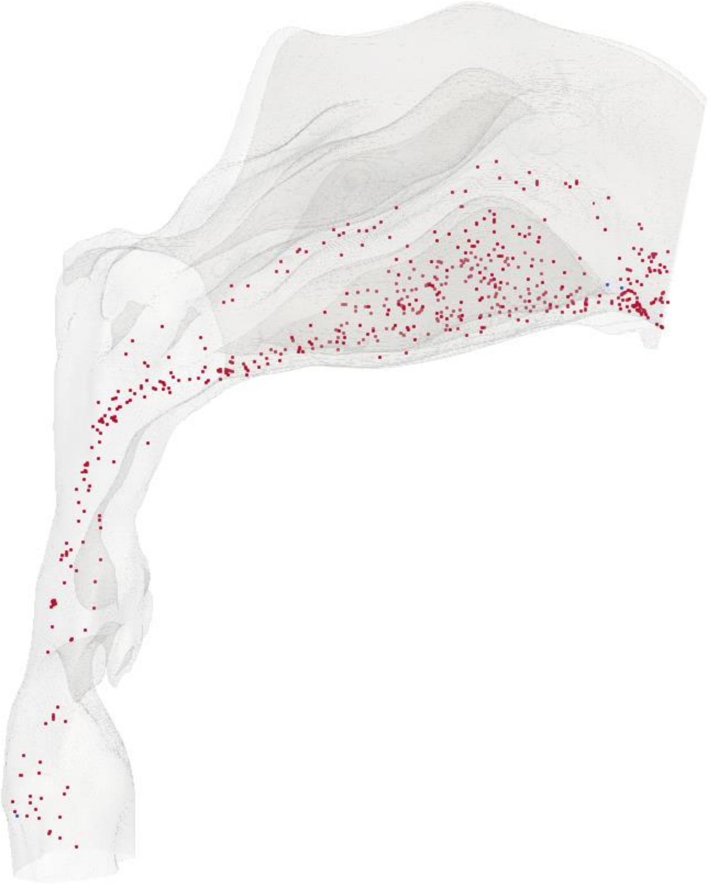

Figure 41: Particle Tracking – 1 µm and 5 l/min – test object A: Red – active (travelling) particles, blue – inactive (stuck) particles

Die approbierte gedruckte Originalversion dieser Diplomarbeit ist an der TU Wien Bibliothek verfügbar
The approved original version of this thesis is available in print at TU Wien Bibliothek.
TU WIEN Bibliothek Your knowledge hub

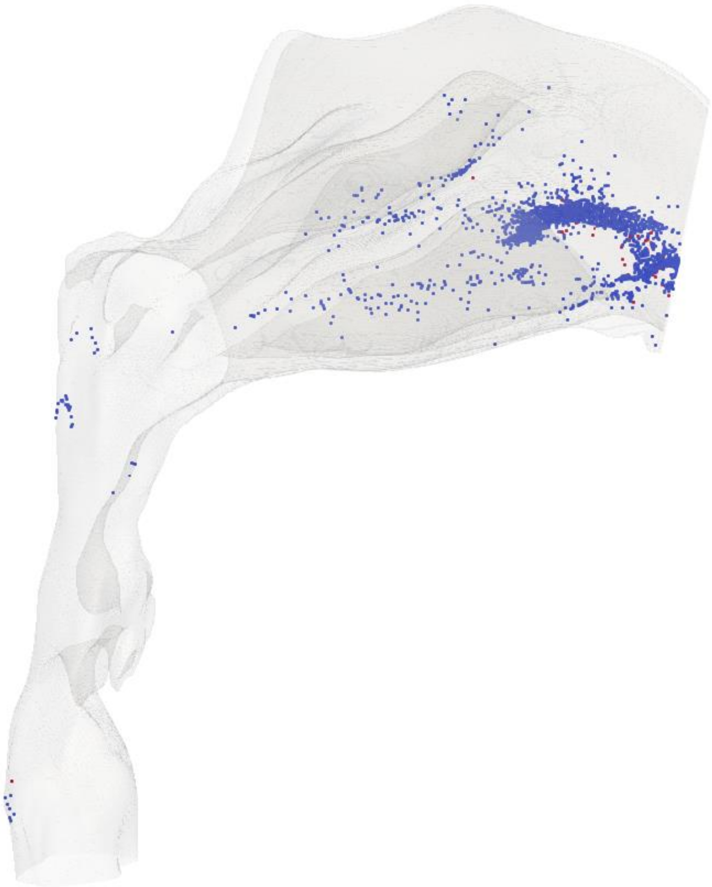

Figure 42: Particle Tracking – 50 µm and 15 l/min – test object A: Red – active (travelling) particles, blue – inactive (stuck) particles

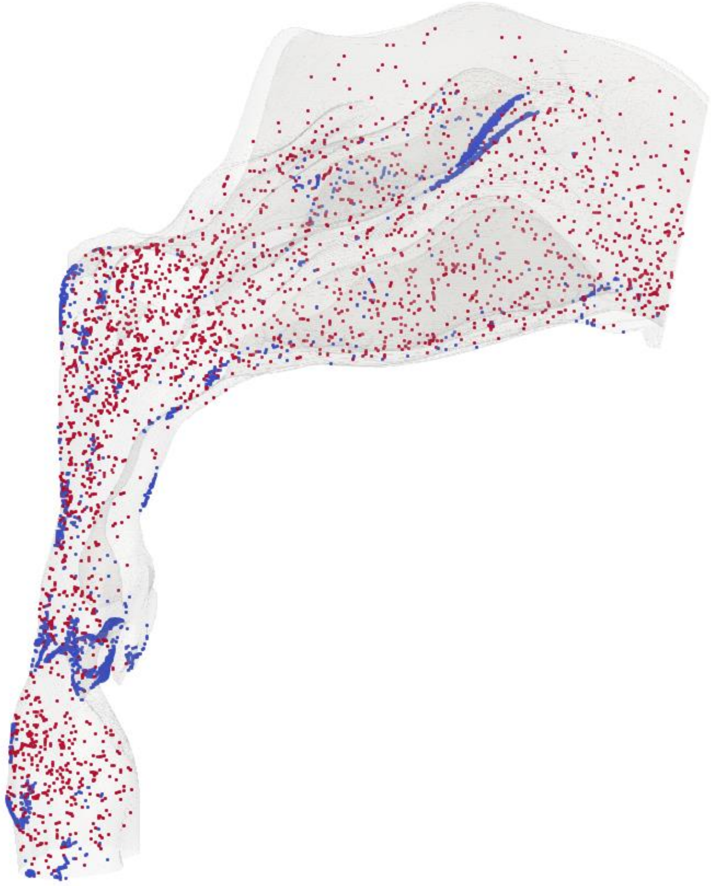

Figure 43: Particle Tracking 10 µm and 20 l/min – test object A: Red – active (travelling) particles, blue – inactive (stuck) particles

Die approbierte gedruckte Originalversion dieser Diplomarbeit ist an der TU Wien Bibliothek verfügbar
The approved original version of this thesis is available in print at TU Wien Bibliothek.
TU Bibliothek WIEN Your knowledge hub

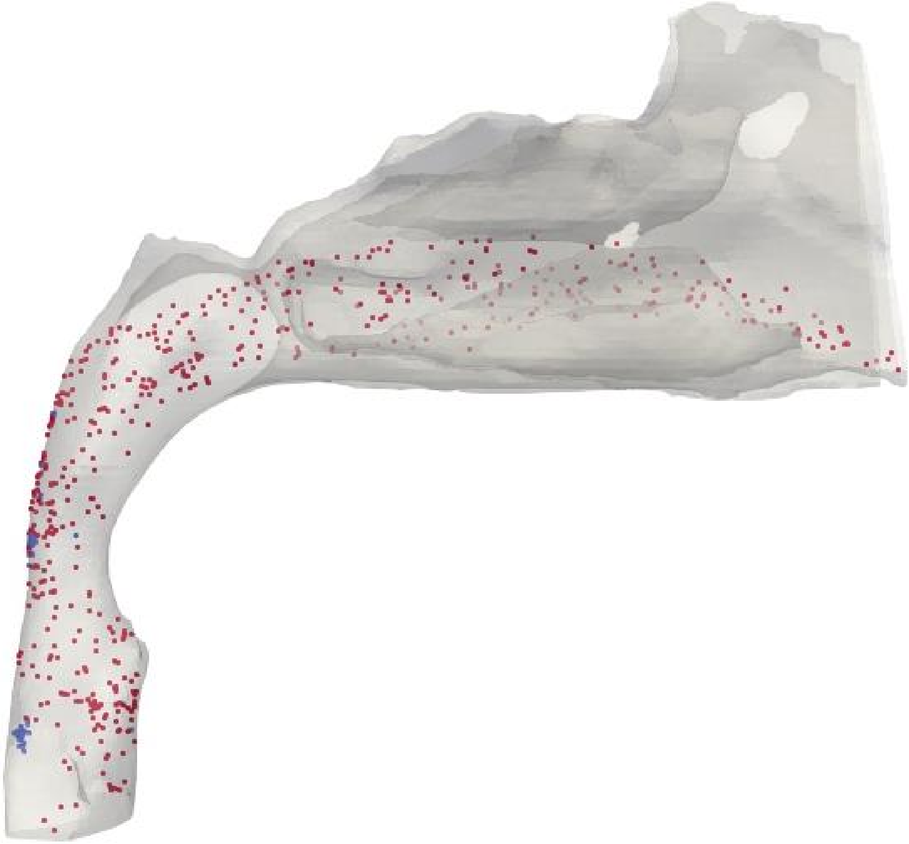

Figure 44: Particle Tracking – 1 µm and 5 l/min – test object B: Red – active (travelling) particles, blue – inactive (stuck) particles

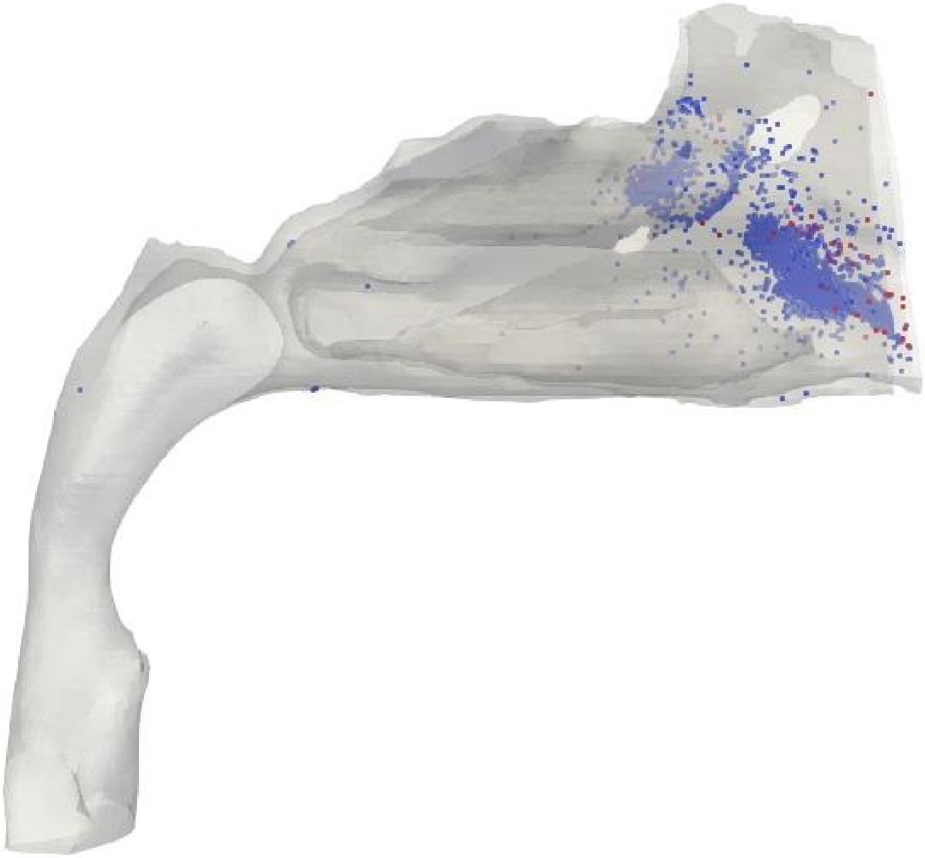

Figure 45: Particle Tracking – 30 µm and 20 l/min – test object B: Red – active (travelling) particles, blue – inactive (stuck) particles

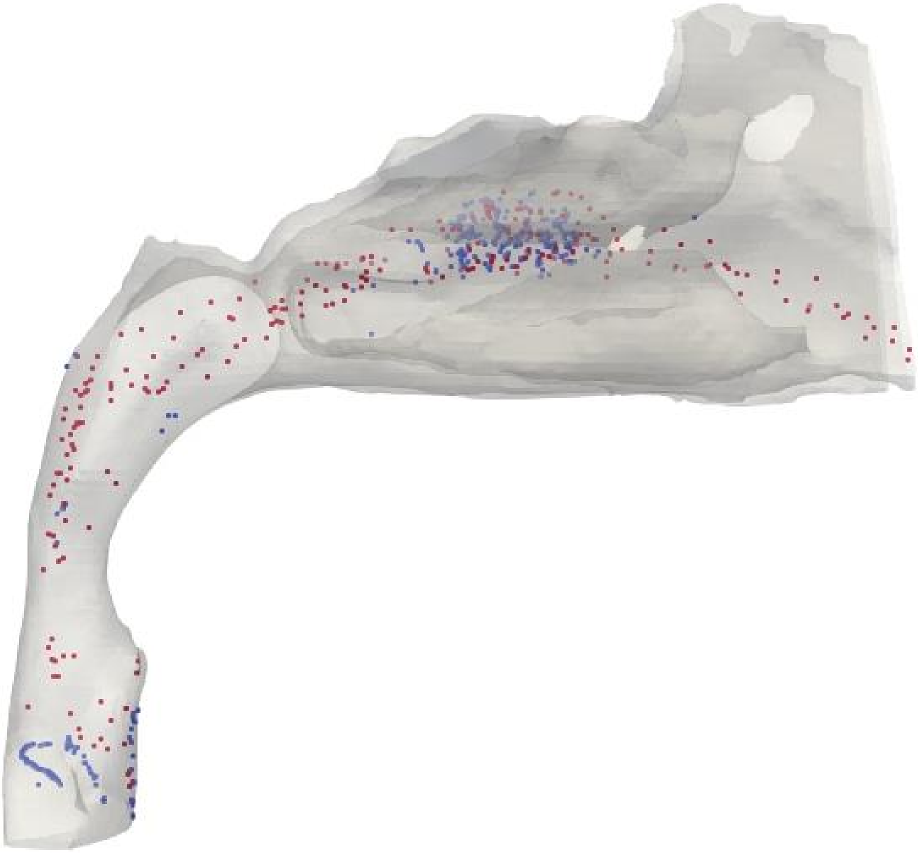

Figure 46: Particle Tracking – 20 µm and 5 l/min – test object B: Red – active (travelling) particles, blue – inactive (stuck) particles

7. Analysis

In this chapter the data obtained by the simulations is analysed. In particular, considerations are made on how the corresponding results depend on different parameters. The chapter is separated in an analysis of the flow and the particle tracking for the different test objects.

7.1 Flow – Test object A

In figure 47 the pressure drop of the different flow simulations (5 l/min, 10 l/min, 15 l/min, 20 l/min) is visualised. With a second order polynomial it is possible to approximate the relation between the flowrate and the pressure drop (see figure 47).

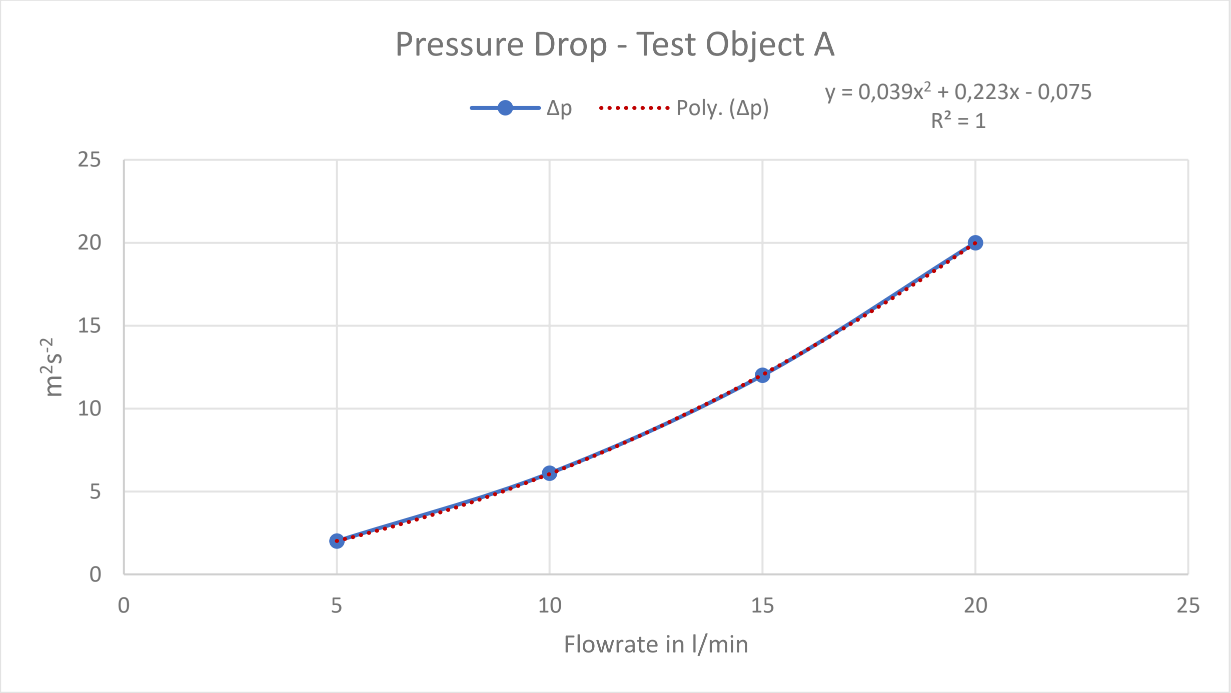

Figure 47: Pressure drop – test object A

7.2 Flow – Test object B

Similarly, it is possible to approximate the pressure drop of test object B with a second order polynomial. The flow simulations were executed with 5 l/min, 10 l/min, 15 l/min, 20 l/min, 60 l/min and 120 l/min.

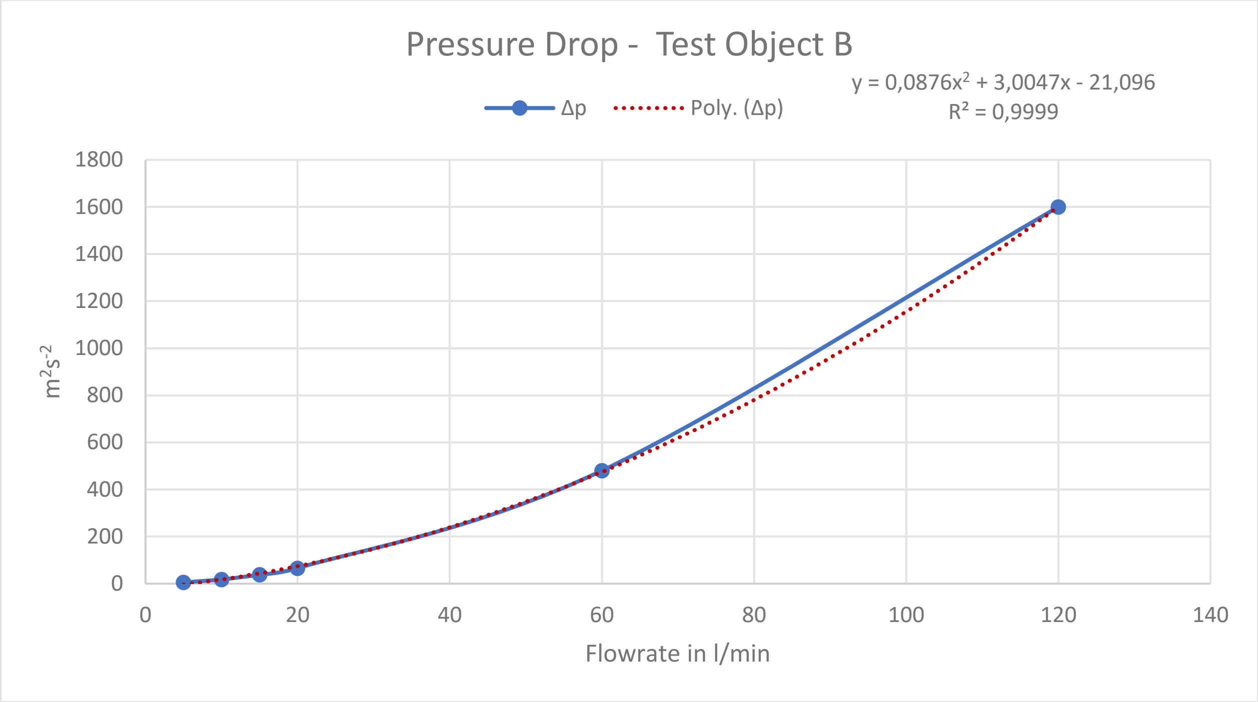

Figure 48: Pressure drop – test object A

When comparing the pressure drops for the same volume flowrates for the different geometries, it is noticeable that the values for test object B are higher. This means that the geometry of test object B causes a higher fluid mechanical resistance.

Flowrate in l/min	5	10	15	20	60	120
Flowrate in cm^{3}s^{-1}	83,3333333	166,666667	250	333,333333	1000	2000
Test object A						
Pressure drop in m^{2}s^{-2}	2	6,1	12	20		
Test object B						
Pressure drop in m^{2}s^{-2}	5,2	18	38	66	480	1600

Table 1: Pressure drop

7.3 Particle Tracking – Test object A

In general, three regions of the geometry were observed (see figure 49). At first the particle tracking in the total nasal interiors was analysed. In addition to that, the volume was divided into two areas: The nasal cavity and the throat.

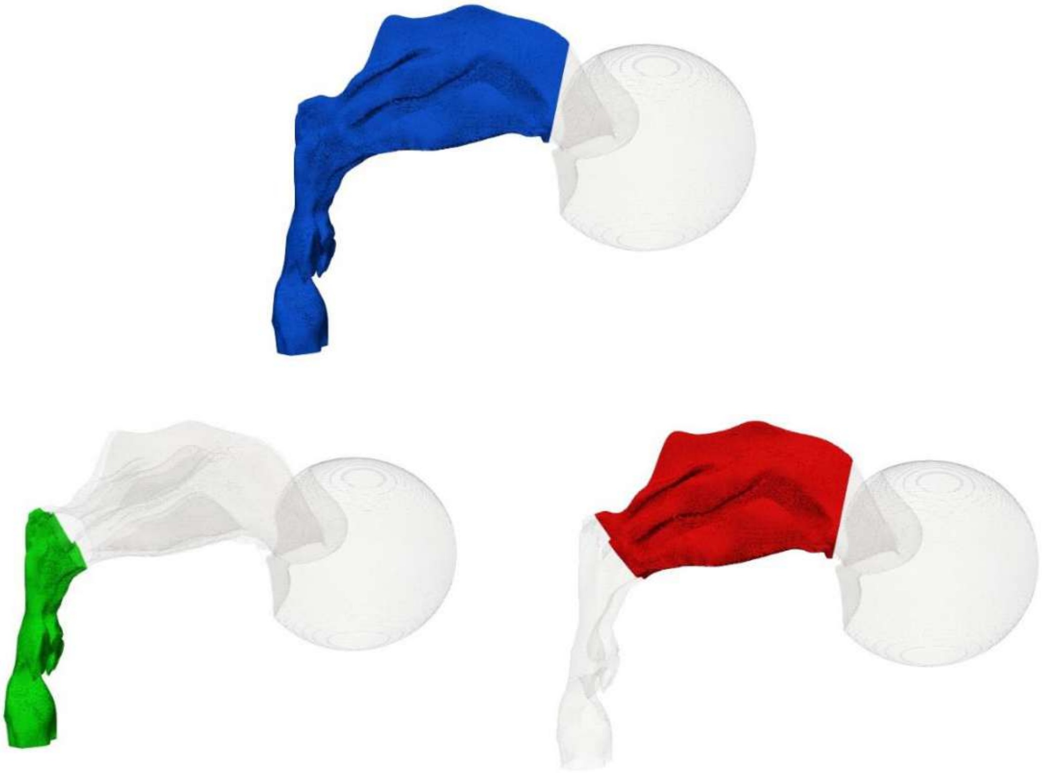

Figure 49: Blue – nasal interiors, green – throat, red – nasal cavity

In table 2 the main data for the particle tracking is presented. (Note: At a flowrate of 20 l/min and a particle size of 50 µm 17900 instead of 19900 particles in a shorter period of time got injected. This change was made to reduce the simulation time.)

Particle size	1 µm			
Flowrate in l/min	5	10	15	20
Flowrate in cm^3s^{-1}	83,3333333	166,666667	250	333,333333
Impaction parameter in $\mu m^2cm^3s^{-1}$	83,3333333	166,666667	250	333,333333

Die approbierte gedruckte Originalversion dieser Diplomarbeit ist an der TU Wien Bibliothek verfügbar
The approved original version of this thesis is available in print at TU Wien Bibliothek.
TU WIEN Bibliothek Your knowledge hub

Particles injected	19900	19900	19900	19900
DF nasal cavity in %	0,41899441	0,98265896	1,86666667	2,789235907
DF throat in %	0,1396648	2,57225434	6,87719298	8,014142605
DF nasal interiors in %	0,55865922	3,55491329	8,74385965	10,8033785
Particle size	5 µm			
Flowrate in l/min	5	10	15	20
Flowrate in cm^{3}s^{-1}	83,3333333	166,666667	250	333,333333
Impaction parameter in µm^{2}cm^{3}s^{-1}	2083,33333	4166,66667	6250	8333,33333
Particles injected	19900	19900	19900	19900
DF nasal cavity in %	0,28490028	0,91580502	2,22002262	3,765608101
DF throat in %	0	4,13589365	9,21945701	12,17186117
DF nasal interiors in %	0,28490028	5,05169867	11,4394796	15,9374693
Particle size	10 µm			
Flowrate in l/min	5	10	15	20
Flowrate in cm^{3}s^{-1}	83,3333333	166,666667	250	333,333333
Impaction parameter in µm^{2}cm^{3}s^{-1}	8333,33333	16666,6667	25000	33333,3333
Particles injected	19900	19900	19900	19900
DF nasal cavity in %	0,73313783	1,75491679	5,62678063	10,84088224
DF throat in %	0,4398827	6,7473525	13,4615385	23,7101221
DF nasal interiors in %	1,17302053	8,50226929	19,0883191	34,5510043
Particle size	20 µm			
Flowrate in l/min	5	10	15	20
Flowrate in cm^{3}s^{-1}	83,3333333	166,666667	250	333,333333
Impaction parameter in µm^{2}cm^{3}s^{-1}	33333,3333	66666,6667	100000	133333,333
Particles injected	19900	19900	19900	19900
DF nasal cavity in %	19,1780822	40,626208	47,1539002	47,3148857
DF throat in %	9,5890411	22,7676846	26,1243851	38,61970907
DF nasal interiors in %	28,7671233	63,3938925	73,2782853	85,9345948
Particle size	30 µm			
Flowrate in l/min	5	10	15	20
Flowrate in cm^{3}s^{-1}	83,3333333	166,666667	250	333,333333
Impaction parameter in µm^{2}cm^{3}s^{-1}	75000	150000	225000	300000
Particles injected	19900	19900	19900	19900
DF nasal cavity in %	49,122807	69,8384201	77,5657555	81,98228314
DF throat in %	9,44669366	13,1059246	12,9448169	12,46866121
DF nasal interiors in %	58,5695007	82,9443447	90,5105725	94,4509443
Particle size	50 µm			
Flowrate in l/min	5	10	15	20
Flowrate in cm^{3}s^{-1}	83,3333333	166,666667	250	333,333333
Impaction parameter in µm^{2}cm^{3}s^{-1}	208333,333	416666,667	625000	833333,333
Particles injected	19900	19900	19900	17900
DF nasal cavity in %	86,9444444	91,0804931	96,7013889	98,68376645
DF throat in %	1,11111111	3,62581581	1,64930556	0,472494094
DF nasal interiors in %	88,0555556	94,7063089	98,3506944	99,1562605

Table 2: Main data for the particle tracking of test object A

7.3.1 Nasal Interiors

The deposition fraction is the main parameter to characterize the ability of particles to pass certain areas. In figure 50 this benchmark is recorded over the impaction parameter. Before an impaction parameter of about 10 000 $\mu m^2 cm^3 s^{-1}$ the deposition fraction is smaller than about 15 %. This means that nearly all particles which enter the nasal interiors (see figure 49) are carried by the air stream through the geometry. In contrast to that an IP over about 300 000 $\mu m^2 cm^3 s^{-1}$ leads to an DF of about 95 %. So almost all particles which enter the nasal interiors get deposited on the wall. Between these two regions is an area, where particles are deposited on the wall, but are also carried by the stream through the nasal interiors.

Moreover, the particle sizes are indicated with different symbols, and it is clear to see that by an increase of the flowrate the impaction parameter and the deposition fraction is rising.

Figure 51 shows the DF over the particle sizes and it can be recognized that when particle sizes are rising the deposition fraction does rise as well. In context of figure 50 again, three areas are visible. The first domain of nearly complete deposition is followed by an area of mixed and an area of nearly full deposition.

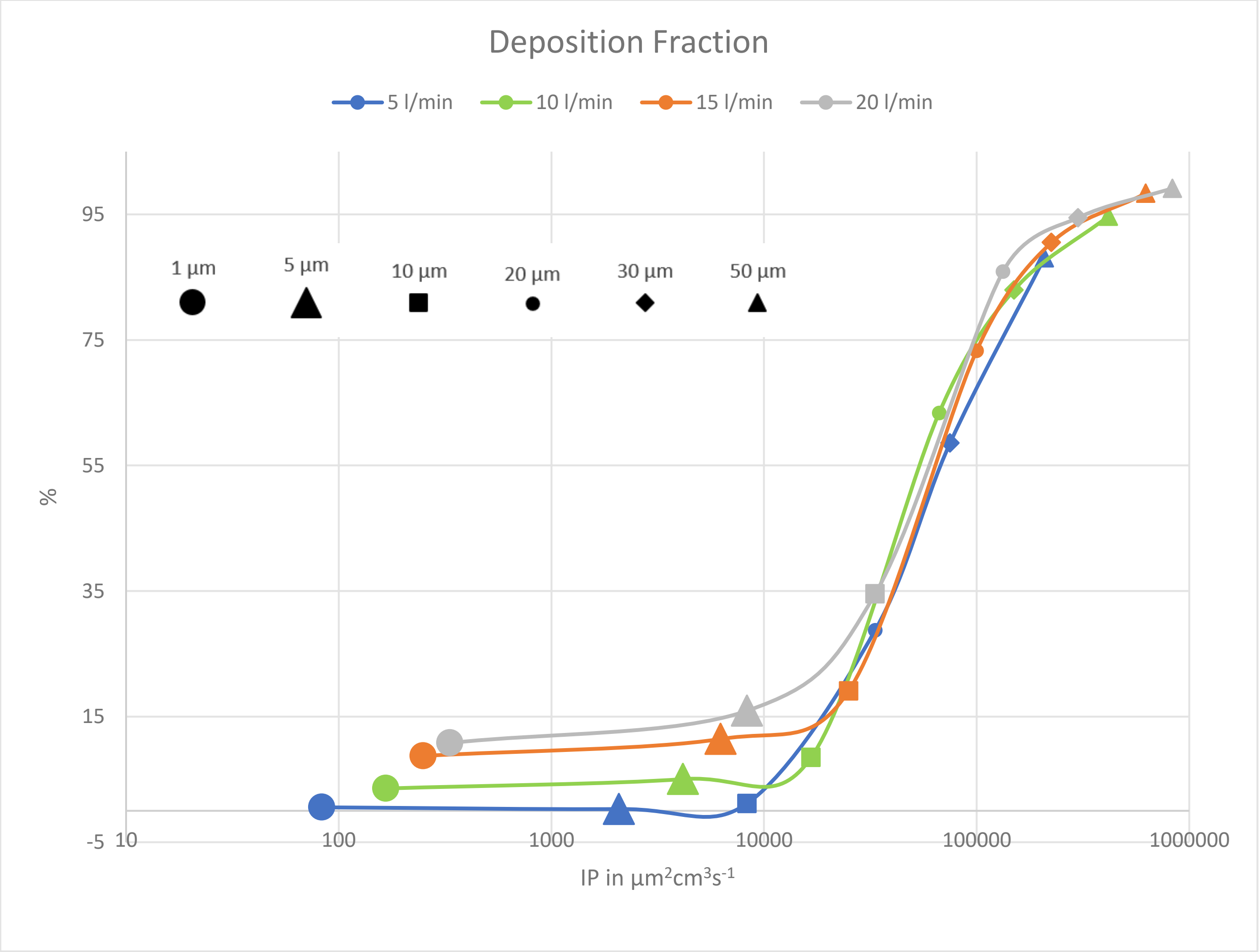

Figure 50: Deposition fraction in dependence of the impaction parameter for different flowrates with indication of the particle sizes – test object A

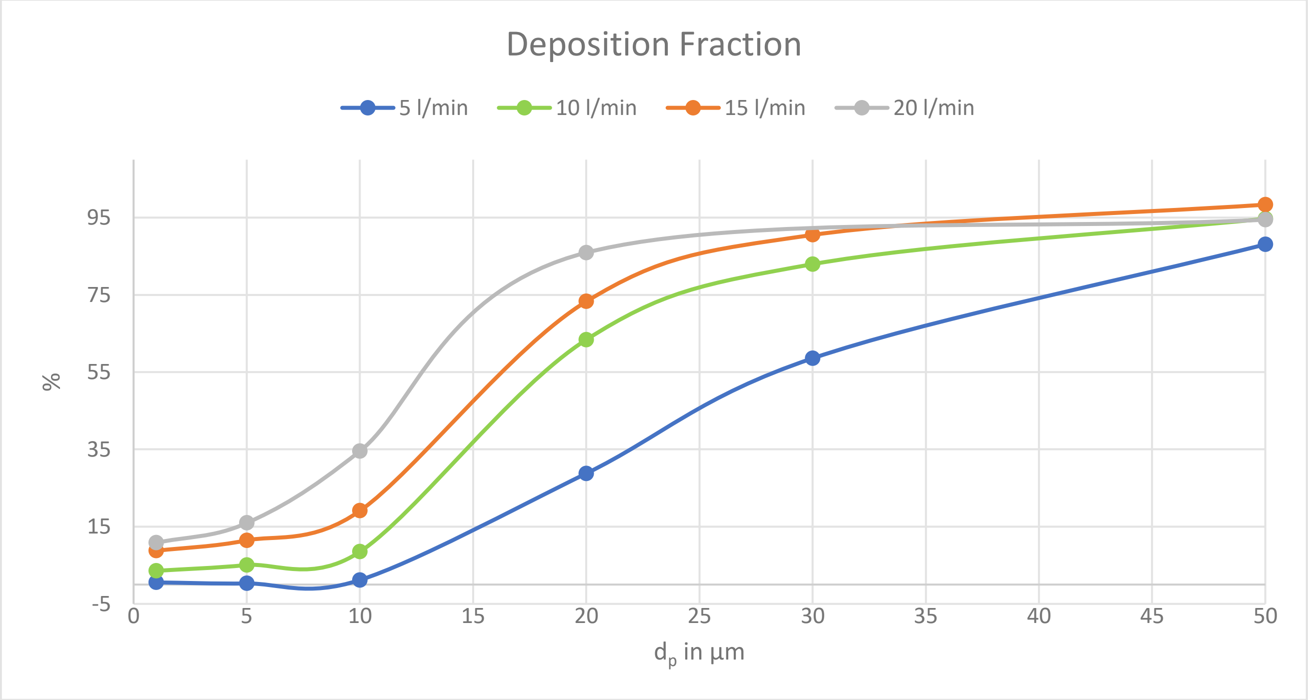

Figure 51: Deposition fraction in dependence of the particle diameter for different flowrates – test object A

To approximate the mixed area a function [1] can be used.

$$\eta = \left(1 - e^{-(a \cdot IP)^b}\right) \qquad (24)$$

This function describes the data points and consists only of the impaction parameter and two constants.

The green line in figure 52 shows the approximation for the simulation data. It can be observed that the function approaches the mixed area in quite a good way. The two constants are figured out by *Matlab*.

$$a = 0{,}00001222$$

$$b = 1{,}071$$

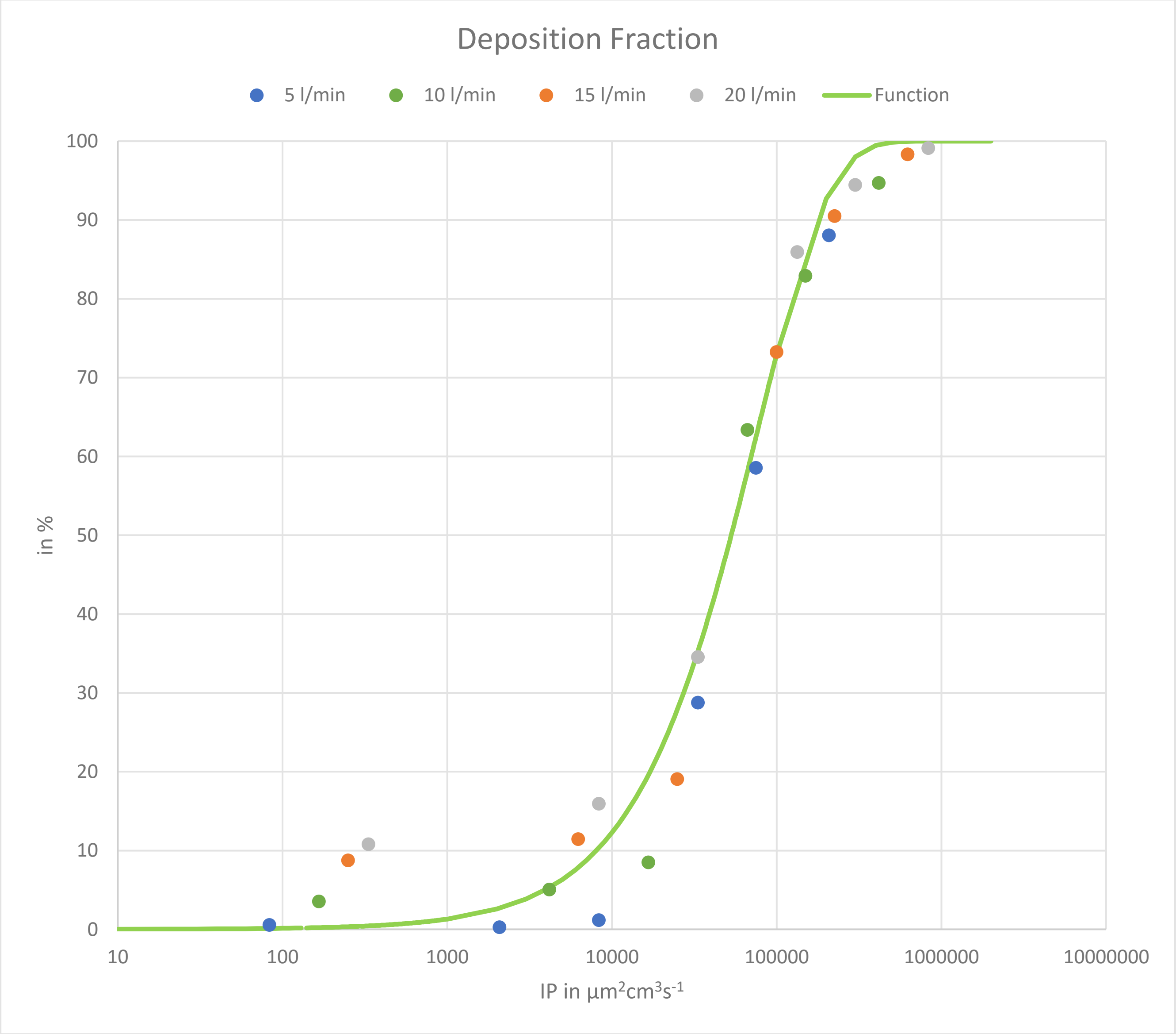

Figure 52: Deposition fraction – approximation – test object A

To validate the simulations figure 53 shows an approximation line of J.T.Kellys experiments [1]. The similarity of the two lines can be seen. To provide an explanation for the difference in space of the functions it should be noted that J.T.Kellys investigated the particle flow with replicas of the nasal interiors. Moreover, the used *MRI* images were of low resolution, which led to high particle deposition in comparison with real nasal interiors [2]. If the deposition fraction is presented in dependence of the impaction parameter, the data can vary a lot [2]. The geometry J.T.Kelly used is different from the nasal interios which was used for this study.

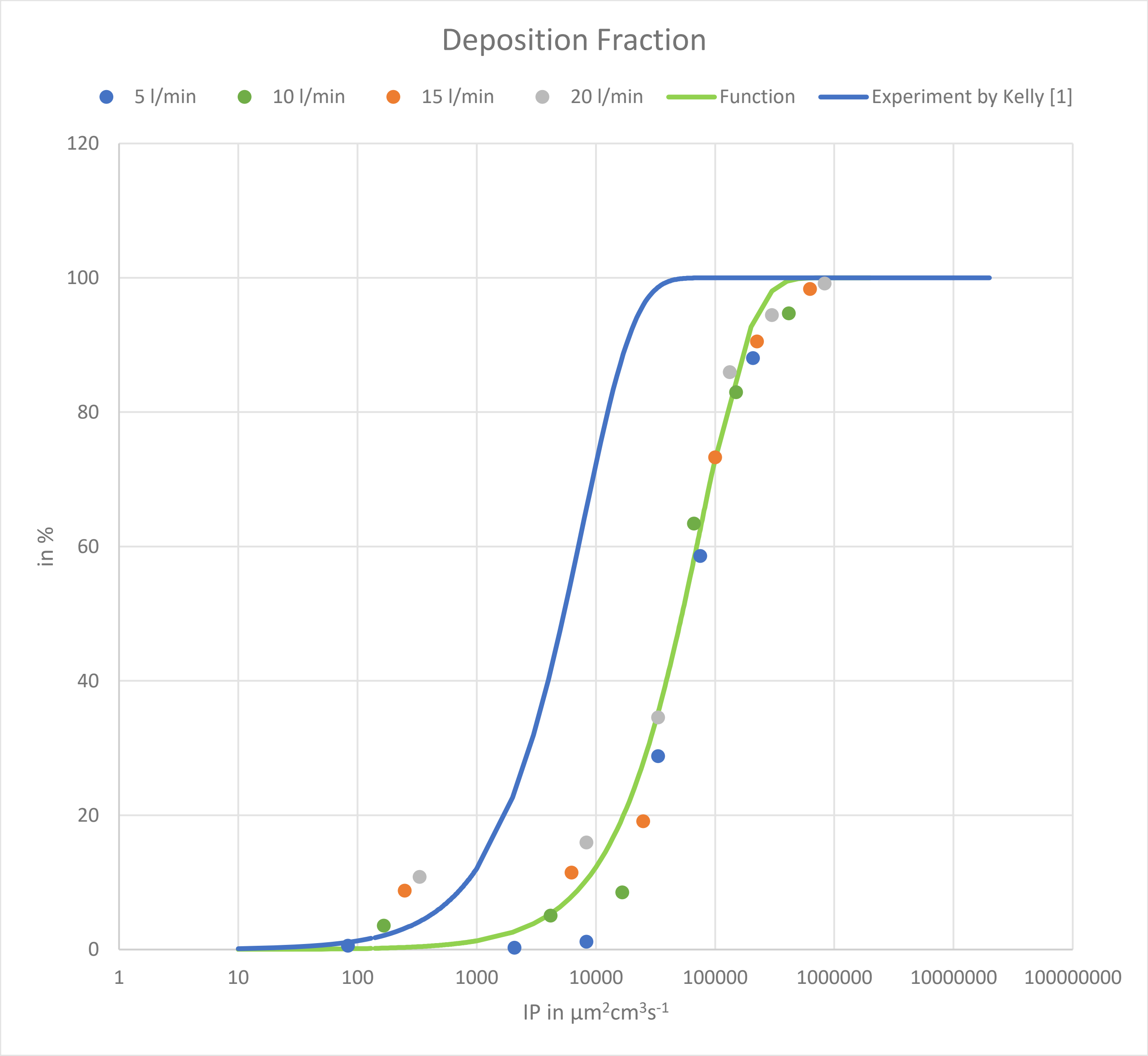

Figure 53: Deposition fraction – comparison – test object A

Die approbierte gedruckte Originalversion dieser Diplomarbeit ist an der TU Wien Bibliothek verfügbar
The approved original version of this thesis is available in print at TU Wien Bibliothek.
TU WIEN Bibliothek Your knowledge hub

Another way to present the particle deposition is *DF* in dependence of $d_p^2\Delta P$ (see figure 54).

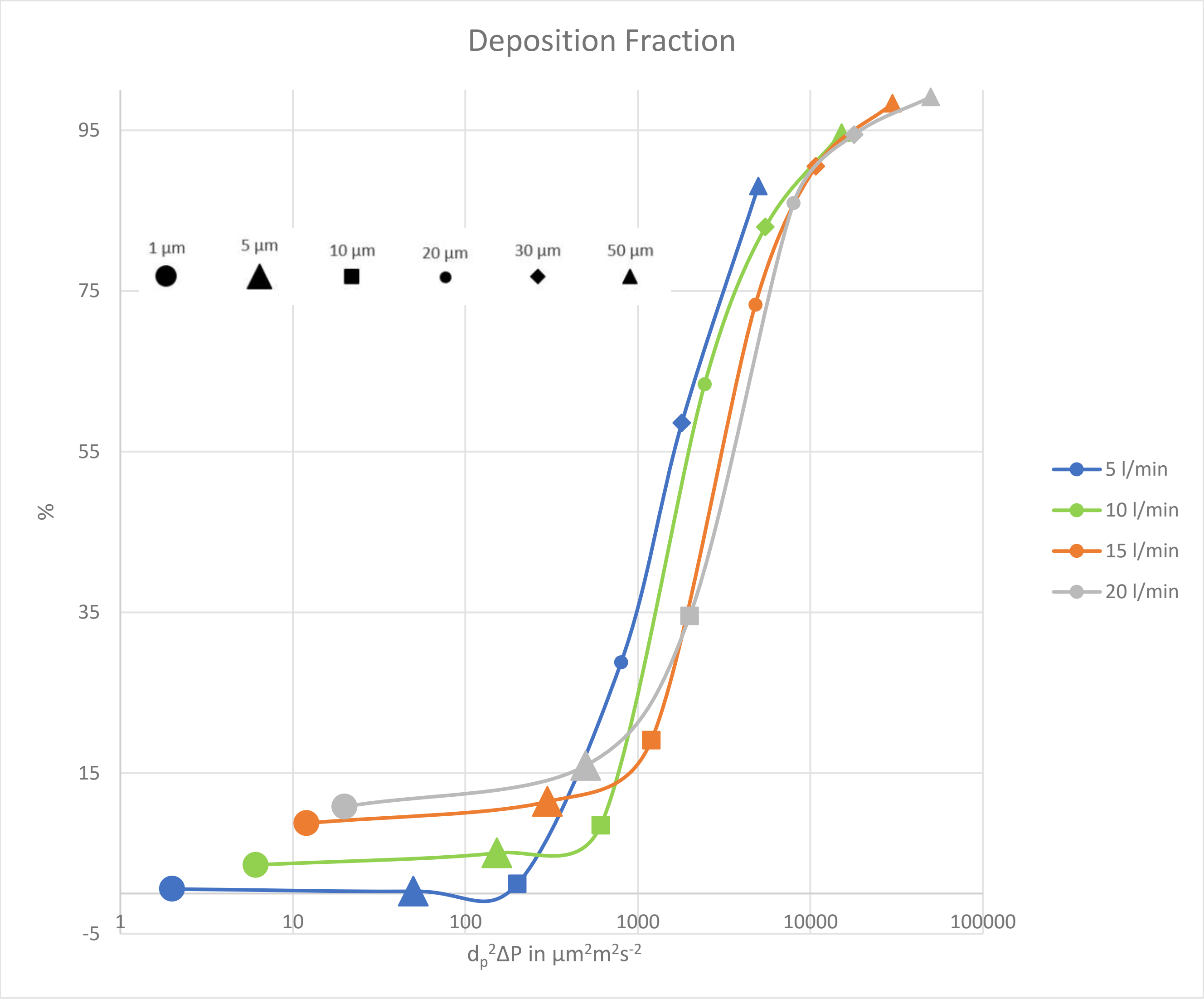

Figure 54: Deposition fraction in dependence of the squared particle diameter times the pressure drop for different flowrates with indication of the particle sizes – test object A

7.3.2 Nasal Subdivision

To achieve a deeper understanding of the particle deposition in the nasal interiors, the nasal geometry A was divided into two subareas (see figure 49). In figure 55 to figure 60 the deposition fraction for the nasal interiors, the nasal cavity and the throat can be seen. In general *DF* is rising with the particle sizes and the flowrates. For small particle sizes (1 to 10 µm) the *DF* is mainly determined by the throat. So, if small particles deposit, they will mainly deposit on the walls in the throat. In contrast to this, larger particle sizes (20 to 50 µm) will collide in the nasal cavity. So, large particles will be separated from the airflow in the beginning of the nasal interiors and small particles are more likely to enter deeper in the nasal airways before they maybe deposit on the wall.

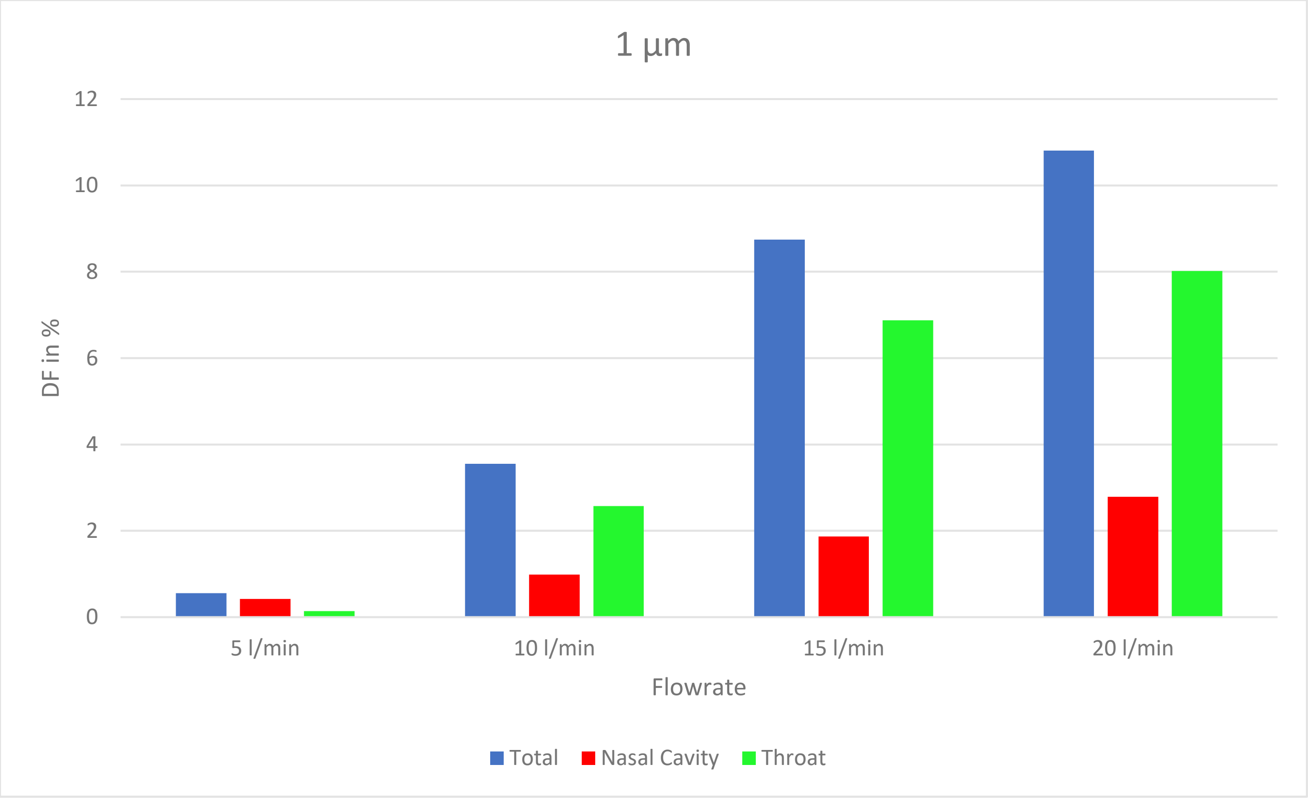

Figure 55: Deposition fraction – 1 µm – test object A

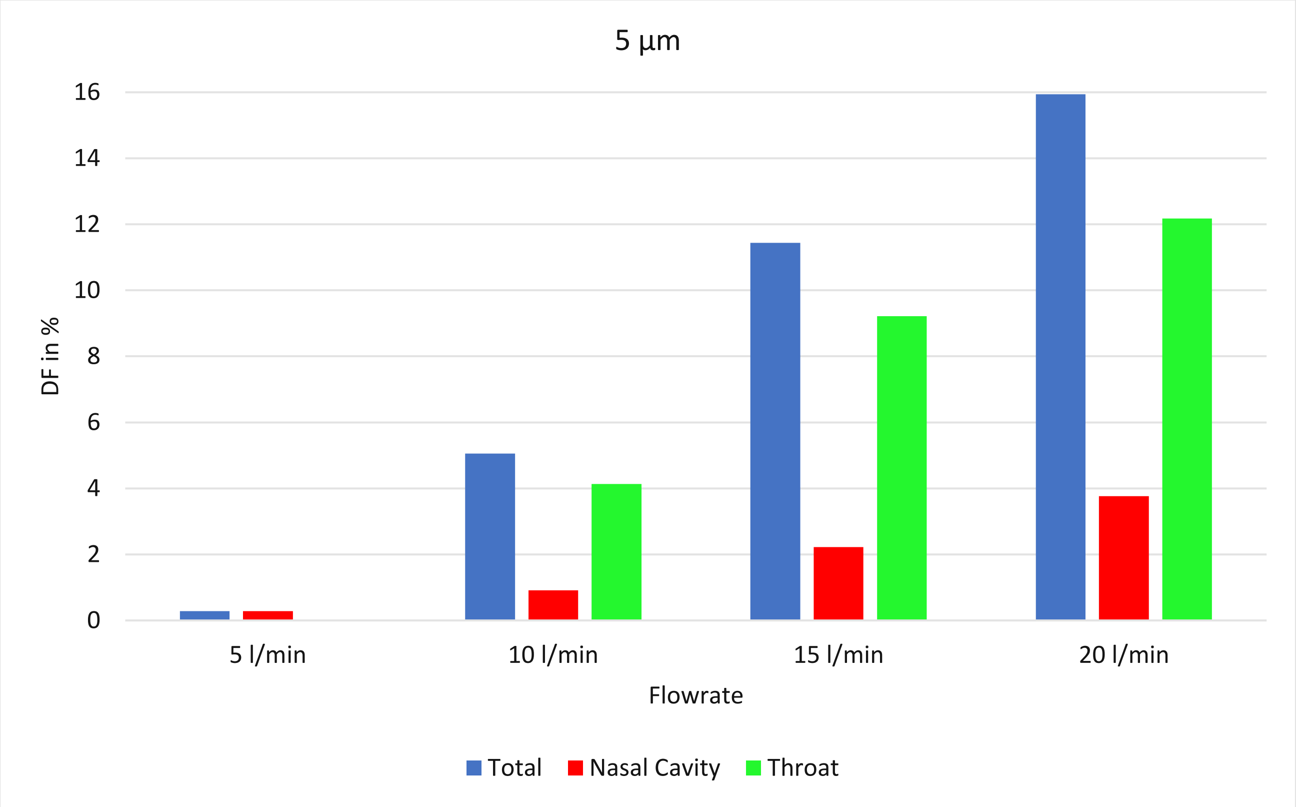

Figure 56: Deposition fraction – 5 µm – test object A

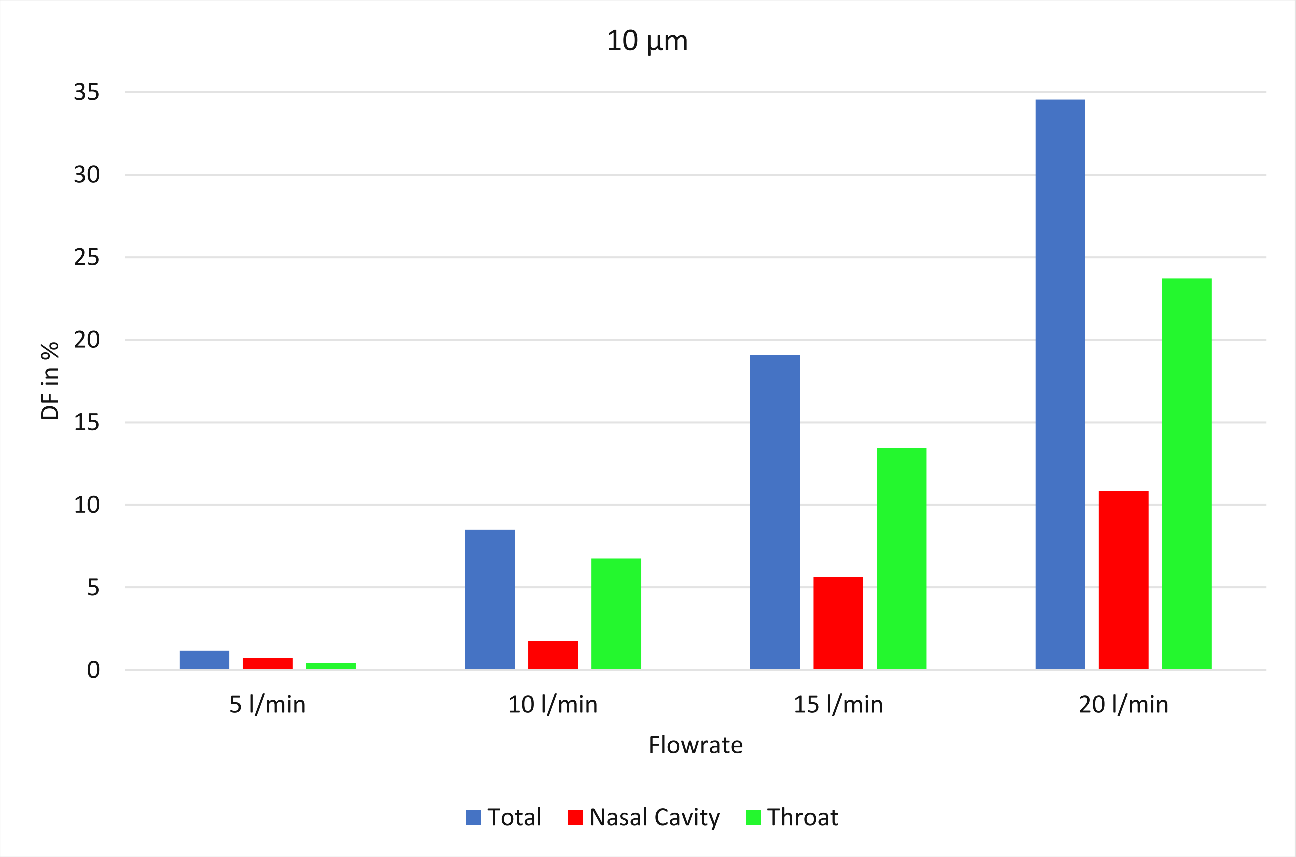

Figure 57: Deposition fraction – 10 µm – test object A

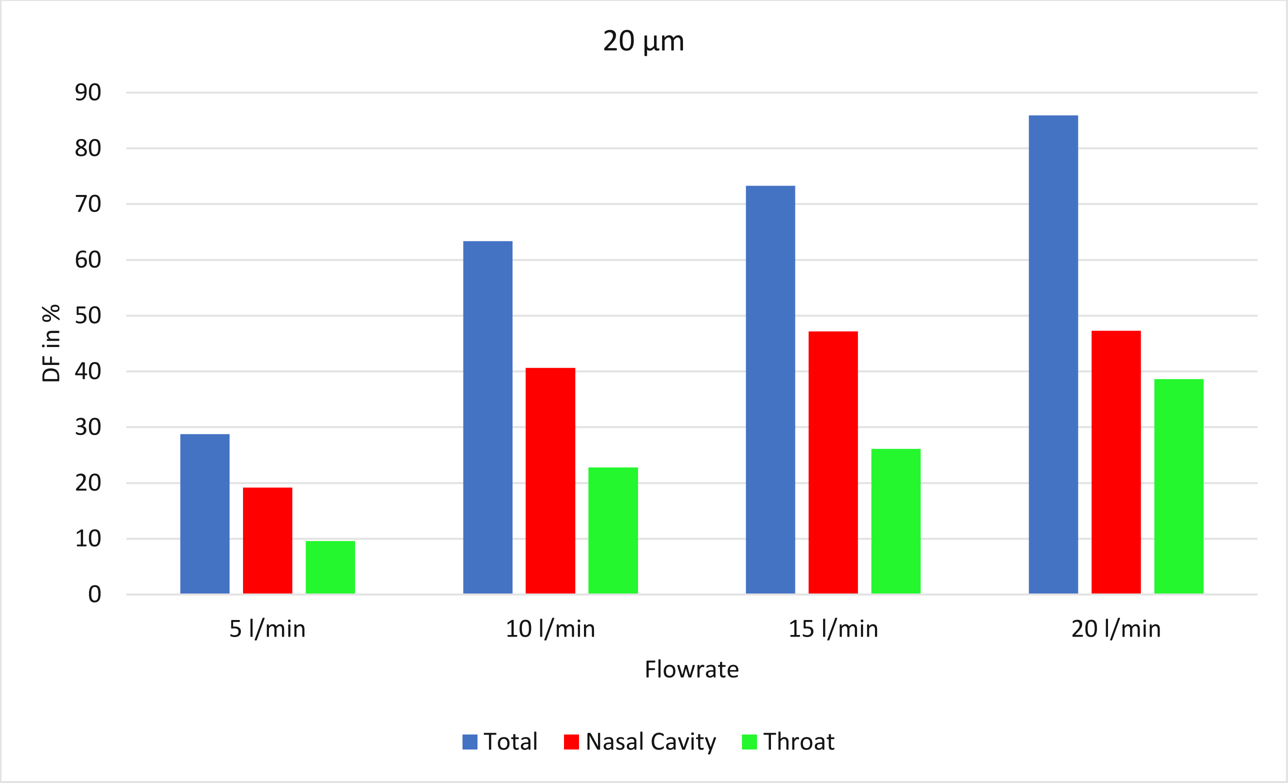

Figure 58: Deposition fraction – 20 µm – test object A

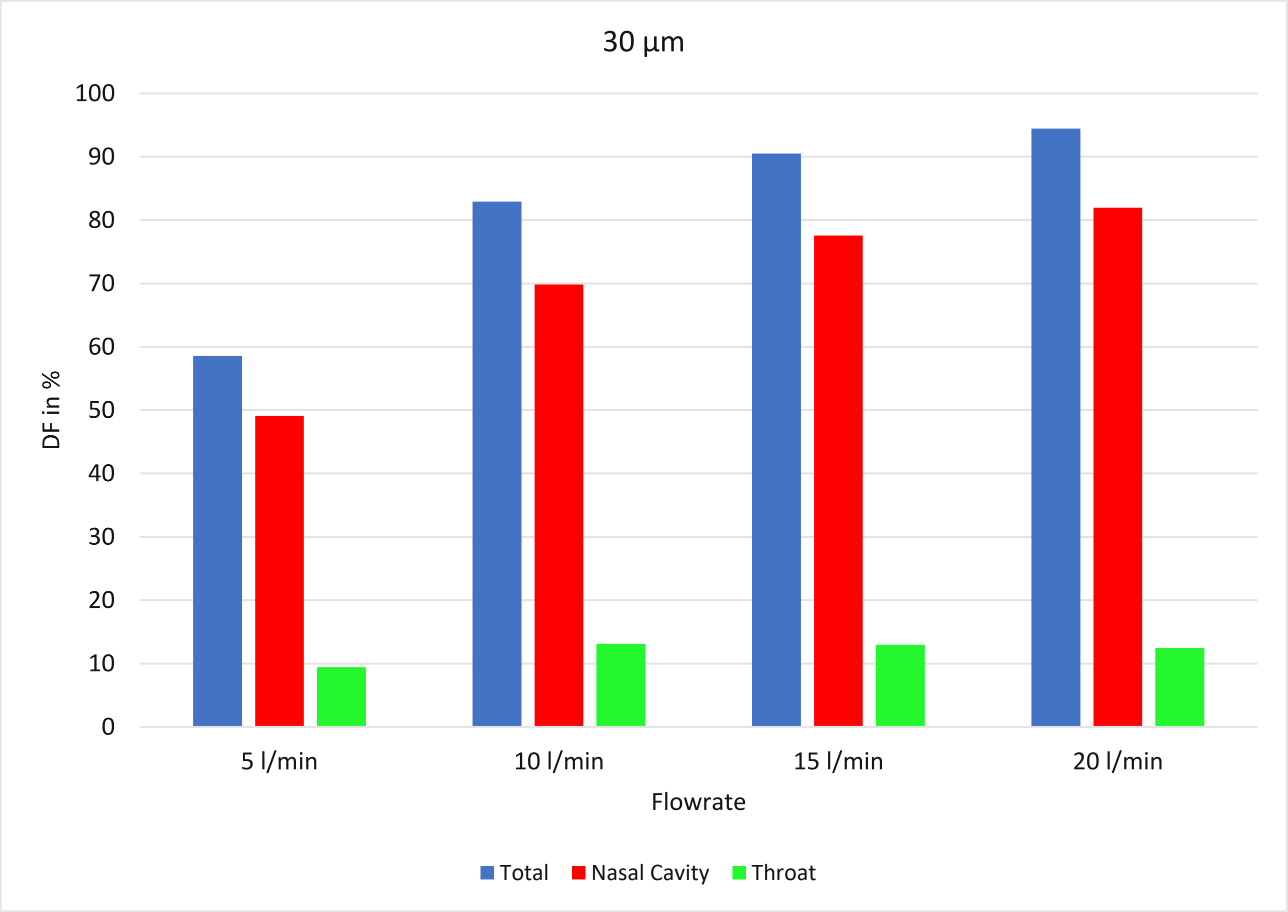

Figure 59: Deposition fraction – 30 µm – test object A

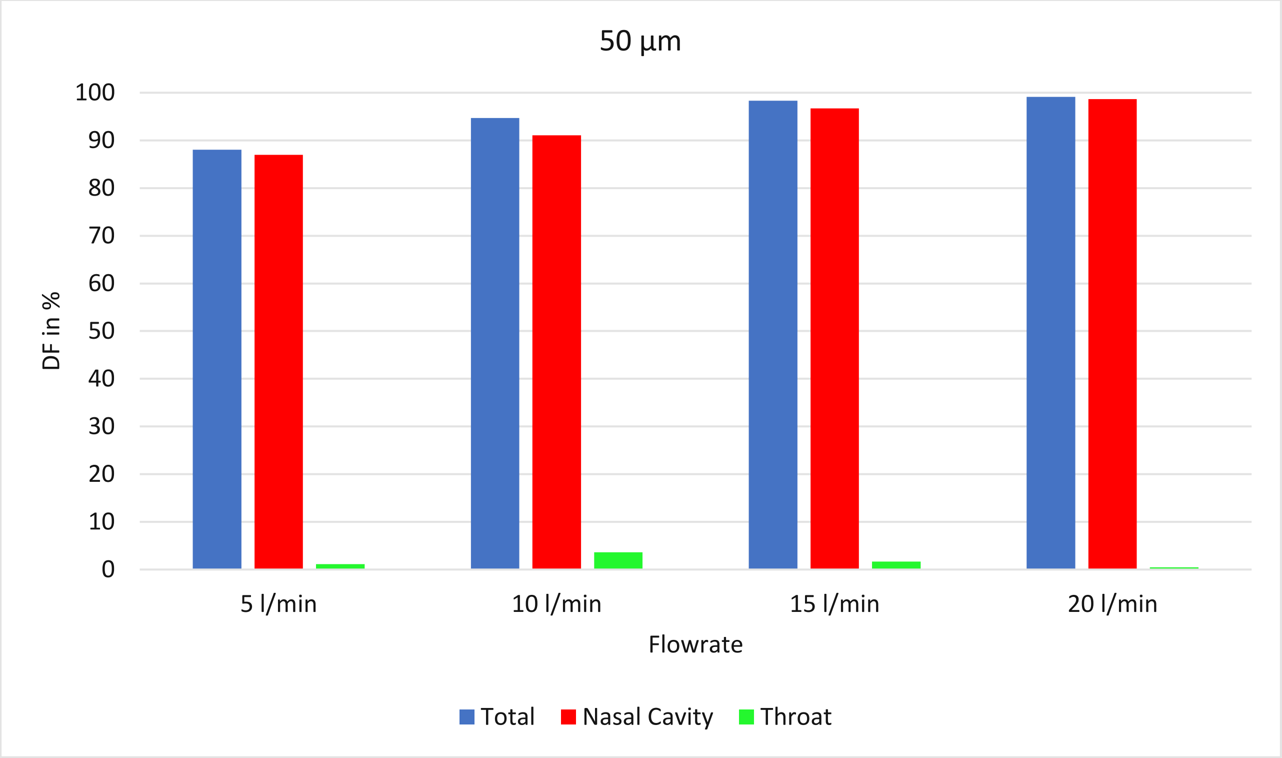

Figure 60: Deposition fraction – 50 µm – test object A

7.4 Particle Tracking – Test object B

The analyses of the particle tracking simulations with test object B were limited to the whole nasal interiors (figure 61).

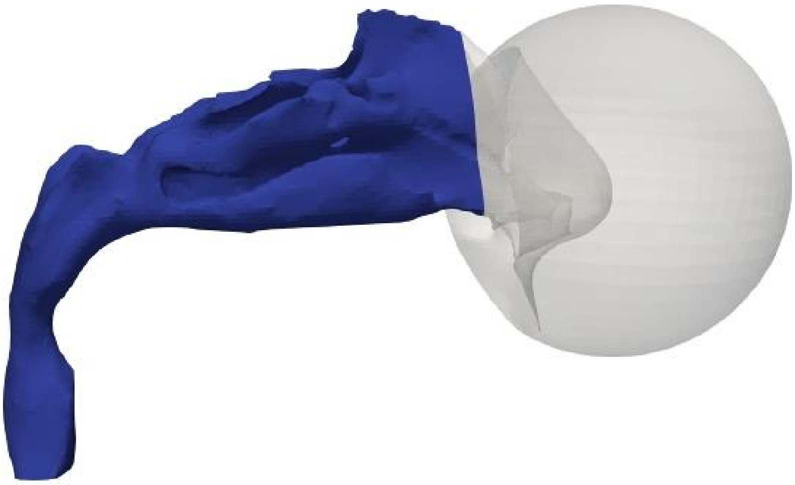

Figure 61: Blue – nasal interiors – test object B

Die approbierte gedruckte Originalversion dieser Diplomarbeit ist an der TU Wien Bibliothek verfügbar
The approved original version of this thesis is available in print at TU Wien Bibliothek.
TU WIEN Bibliothek Your knowledge hub

In table 3 the main data for the particle tracking of test object B is shown. (Note: At a flowrate of 20 l/min and a particle size of 50 µm 17900 instead of 19900 particles in a shorter period of time got injected. This change was made to reduce the simulation time.)

Particle size	1 µm	
Flowrate in l/min	5	20
Flowrate in cm^3s^{-1}	83,3333333	333,333333
Impaction parameter in $\mu m^2cm^3s^{-1}$	83,3333333	333,333333
Particles injected	19900	19900
DF nasal interiors in %	4,05904059	17,3036768
Particle size	5 µm	
Flowrate in l/min	5	20
Flowrate in cm^3s^{-1}	83,3333333	333,333333
Impaction parameter in $\mu m^2cm^3s^{-1}$	2083,33333	8333,33333
Particles injected	19900	19900
DF nasal interiors in %	5,16324981	40,13332116
Particle size	10 µm	
Flowrate in l/min	5	20
Flowrate in cm^3s^{-1}	83,3333333	333,333333
Impaction parameter in $\mu m^2cm^3s^{-1}$	8333,33333	33333,3333
Particles injected	19900	19900
DF nasal interiors in %	6,124234471	87,67845776
Particle size	20 µm	
Flowrate in l/min	5	20
Flowrate in cm^3s^{-1}	83,3333333	333,333333
Impaction parameter in $\mu m^2cm^3s^{-1}$	33333,3333	133333,333
Particles injected	19900	19900
DF nasal interiors in %	51,13122172	99,3188163
Particle size	30 µm	
Flowrate in l/min	5	20
Flowrate in cm^3s^{-1}	83,3333333	333,333333
Impaction parameter in $\mu m^2cm^3s^{-1}$	75000	300000
Particles injected	19900	19900
DF nasal interiors in %	91,17647059	99,16635791
Particle size	50 µm	
Flowrate in l/min	5	20
Flowrate in cm^3s^{-1}	83,3333333	333,333333
Impaction parameter in $\mu m^2cm^3s^{-1}$	208333,333	833333,333
Particles injected	19900	17900
DF nasal interiors in %	95,56213018	99,28628073

Table 3: Main data for the particle tracking of test object B

The deposition fraction in dependence of the impaction parameter for test object B is shown in figure 62. In comparison with the deposition fraction of test object A it is clear to see that the two characteristics are in the same scale of 100 to 1 000 000 µm^{2}cm^{3}s^{-1}. This is another indication of the validity of this study. Again, three main regions are visible: The first area of the characteristic (figure 62) indicates a range whereby a low percentage of particles which enter the geometry inlet collide with the nasal walls and remain stuck. Following this, the next domain is between about 20 000 to 100 000 µm^{2}cm^{3}s^{-1}, where particles travel through the nasal interiors but also get stuck. In the end after about 100 000 µm^{2}cm^{3}s^{-1} nearly all particles collide with the nasal interiors. As with the diagram of the DF of test object A the symbols represent the different particle sizes and by an increase of the flowrate the impaction parameter and the deposition fraction are rising as well.

In figure 63 the DF in dependence of the particle sizes for different flowrates is shown. It can be seen that when particle sizes are rising, the deposition fraction also does. Furthermore, the similarity with the same kind of diagram for test object A (figure 51) is recognizable.

The deposition fraction in dependence of $d_p^2\Delta P$ is shown in figure 64. Again, ranges of full, nearly none and mixed deposition are visible.

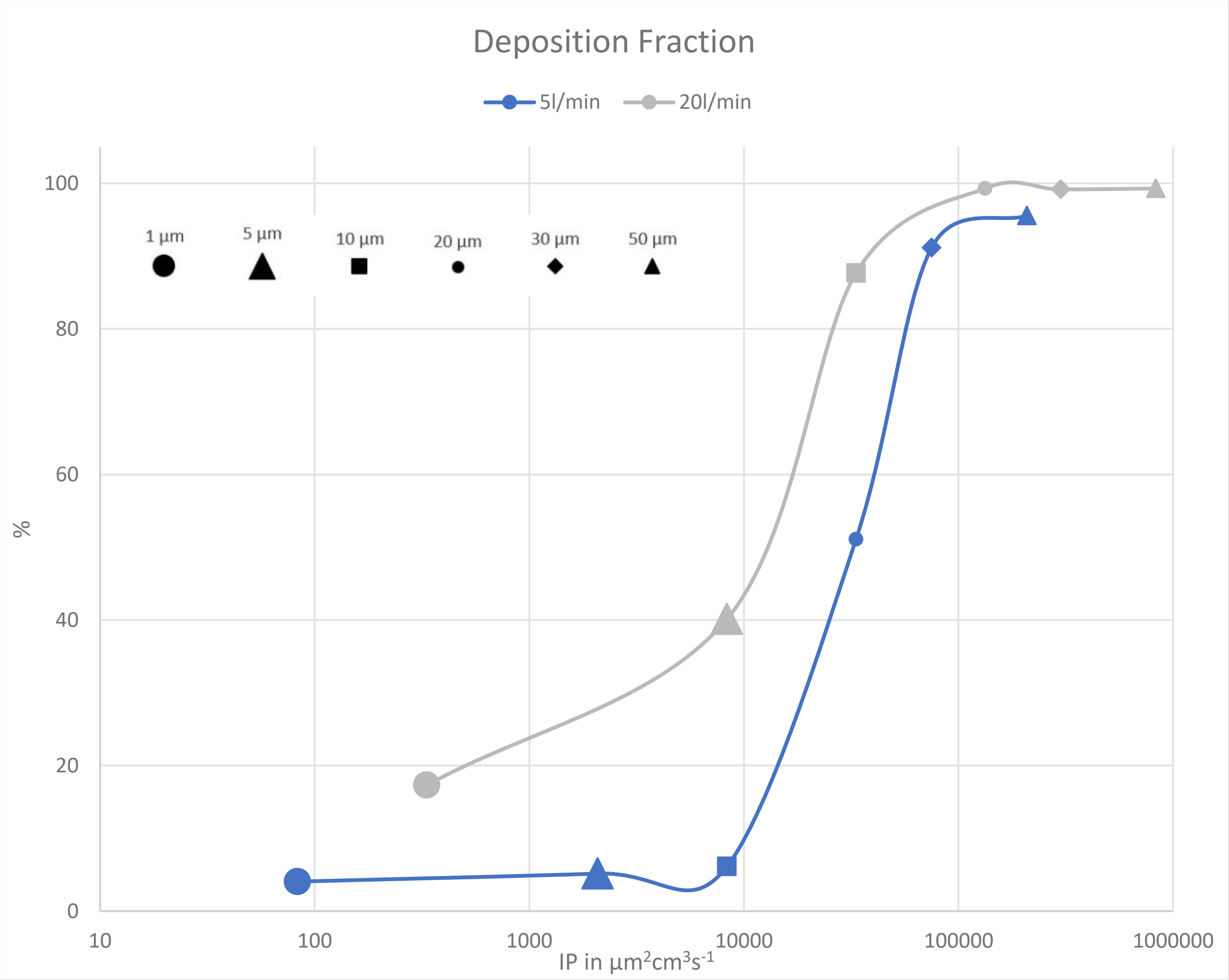

Figure 62: Deposition fraction in dependence of the impaction parameter for different flowrates with indication of the particle sizes – test object B

Die approbierte gedruckte Originalversion dieser Diplomarbeit ist an der TU Wien Bibliothek verfügbar
The approved original version of this thesis is available in print at TU Wien Bibliothek.
TU WIEN Bibliothek Your knowledge hub

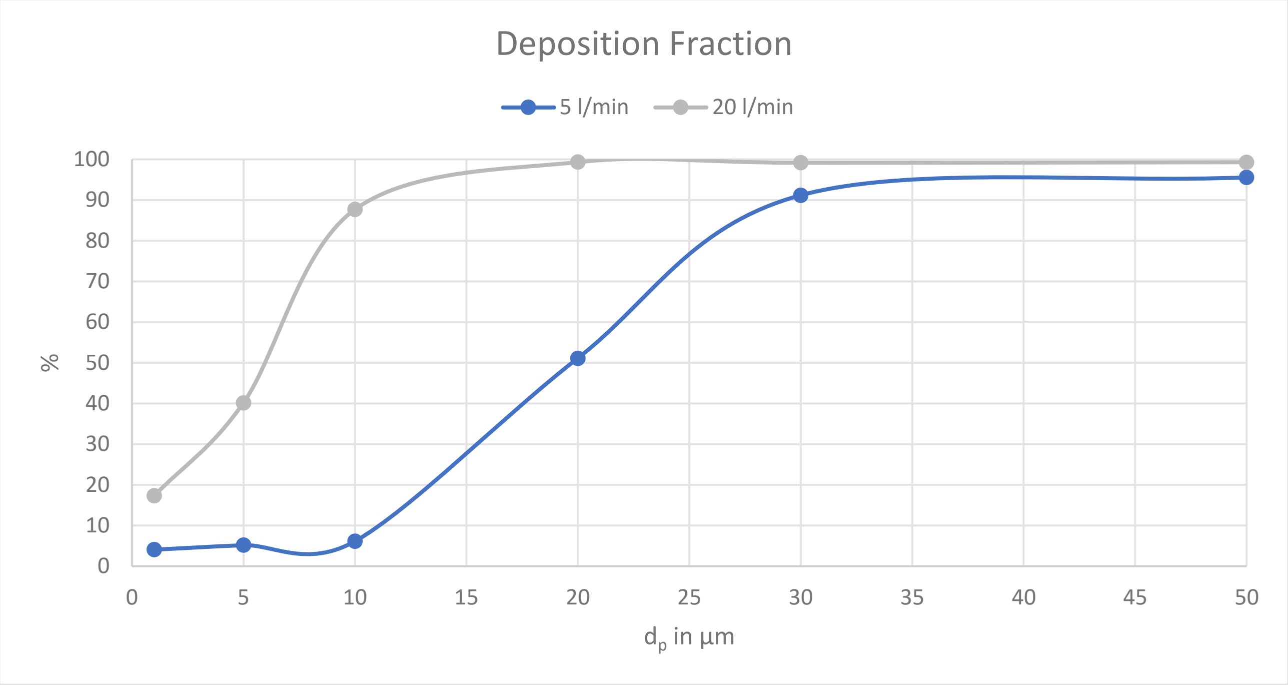

Figure 63: Deposition fraction in dependence of the particle diameter for different flowrates – test object B

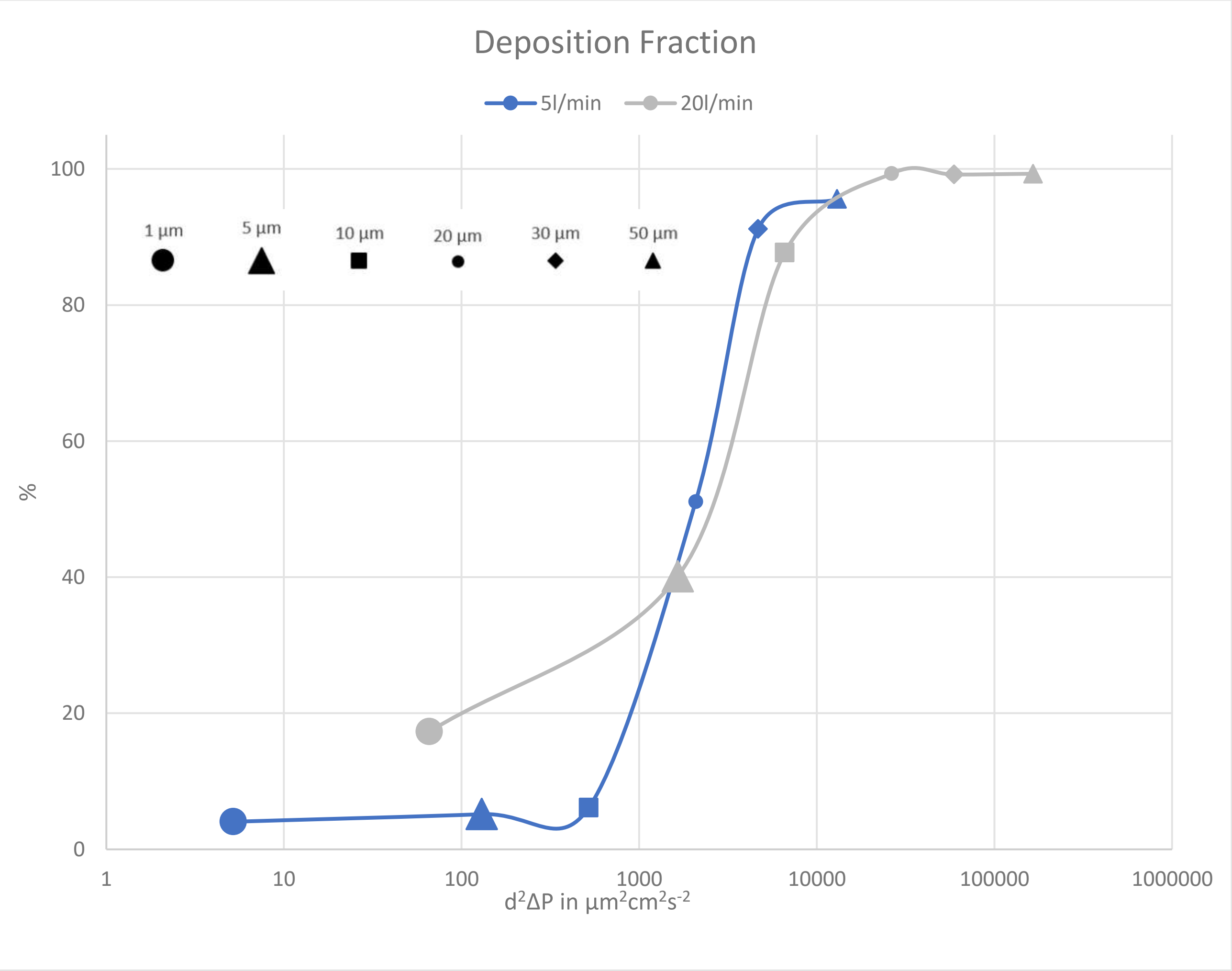

Figure 64: Deposition fraction in dependence of the squared particle diameter times the pressure drop for different flowrates with indication of the particle sizes – test object B

7.5 Comparison of test object A and B

The shown diagrams of test object A and B indicate a strong similarity. The main diagrams, the deposition fraction in dependence of the impaction parameter, are in the same scale. In general, the DF of the nasal interiors B takes on higher values with the same impaction parameter. This means that the geometry leads to full deposition sooner. This observation is also visible in the diagrams of the deposition fraction in dependence of the particle sizes. For example, particles with a size of 20 µm and carried by a flowrate of 5 l/min leads in the geometry of test object A to a DF of about 30 % and in geometry B to a DF of about 50 %. The same particle size carried by a flowrate of 20 l/min leads in the nasal interiors A to a DF of about 86 % and with test object B to a DF of about 100 %.

This shows that the impaction parameter is a good indicator for the behaviour of particle deposition for different particle streams through nasal interiors. When an accurate prediction of the deposition rate is needed, the geometry of the nasal interiors has to be considered.

TU WIEN Bibliothek Your knowledge hub
Die approbierte gedruckte Originalversion dieser Diplomarbeit ist an der TU Wien Bibliothek verfügbar
The approved original version of this thesis is available in print at TU Wien Bibliothek.

8. Conclusion

The aim of this work is to get a better understanding of the fluid mechanic characteristics in the nasal interiors. More specifically, the behaviour of particles of various sizes and different carrier flows got investigated. Furthermore, two nasal interiors got observed. The work shows the dependence of the particle deposition from different parameters. In conclusion, it can be underlined that particles of a higher mass and velocity get deposited in the beginning of the nasal airways versus particles with a low mass and velocity which can flow through the nasal interiors. In between the two stated areas of deposition, there is an area by which some particles deposit and the rest gets carried by the stream through the geometry. In general, the deposition process starts when the carrier stream is no longer able to carry the particles through the complex nasal geometry. This means they leave the stream and collide with the nasal walls. The nasal walls are sticky so the particles adhere on the interfaces. Moreover, the study shows that even with different nasal geometries, the dependence of the particle deposition on the impaction parameter is similar to each other.

This knowledge benefits us as it can be applied for technical applications. For example, nasal sprays can be designed to produce drops with a certain diameter carried by a stream with a certain flowrate. In effect, drugs could be delivered in the most efficient way to regions in the nasal interiors or further in the respiratory system.

Die approbierte gedruckte Originalversion dieser Diplomarbeit ist an der TU Wien Bibliothek verfügbar
The approved original version of this thesis is available in print at TU Wien Bibliothek.
TU WIEN Bibliothek Your knowledge hub

Bibliography

[1] Kelly, J. T.; Asgharian, B.; Kimbell, J. S.; Wong, B. A.: Particle Deposition in Human Nasal Airway Replicas Manufactured by Different Methods. Part I: Inertial Regime Particles. Aerosol Science and Technology, 38:11, 1063-1071, 2004.

[2] Ghalati, P. F.; Keshavarzian, E.; Abouali, O.; Faramarzi, A.; Tu, J.; Shakibafard, A.: Numerical analysis of micro- and nano-particle deposition in a realistic human upper airway, Computers in Biology and Medicine 42, 39-49, 2011.

[3] Calmet, H.; Kleinstreuer, C.; Houzeaux, G.; Kolanjiyil, A.V.; Lehmkuhl, O.; Olivares, E.; Vázquez, M.: Subject-variability effects on micron particle deposition in human nasal cavities, Journal of Aerosol Science 115, 12-28, 2018.

[4] Calmet, H.; Houzeaux, G.; Vázquez, M.; Eguzkitza, B.; Gambaruto, A.M.; Bates, A.J.; Doorly, D.J.: Flow features and micro-particle deposition in a human respiratorysystem during sniffing, Journal of Aerosol Science 123, 171-184, 2018.

[5] Siu, J.; Douglas, R.; Singh, N.; Wong, E.: Anatomy and Physiology of the Human Nose *in* Clinical and Biomedical Engineering in the Human Nose, Springer Nature Singapore, ISBN 978-981-15-6715-5, 2021.

[6] Doorly, D.; Taylor, D.; Gambaruto, A.; Schroter, R.; Tolley, N.: Nasal Architecture: Form and Flow. Philosphical Transactions of the Royal Society, 366:3225-3246, 2008.

[7] Peters, F.; Groß T. F.: Flow characteristics of the nasal cavity. Springer Verlag, 2012.

[8] Armstrong, M.; Walker, S.; Mains, J.; Wilson, C.G.; Drug Delivery Across the Nasal Mucous *in* Mucoadhesive Materials and Drug Delivery Systems, John Wiley & Sons, ISBN 978-1-119-94143-9, 2014.

[9] Schwarze, R.: CFD-Modellierung, Springer Verlag Berlin Heidelberg, ISBN 978-3-642-24377-6, 2013.

[10] Ghaib, K.: Einführung in die numerische Strömungsmechanik. Springer Fachmedien Wiesbaden, ISBN: 978-3-658-26922-7, 2019.

[11] OpenCFD Ltd: Website: www.openfoam.com, [online] https://www.openfoam.com/documentation/guides/latest/doc/guide-applications-solvers-incompressible-simpleFoam.html, 2022. Access on 16.09.2022.

[12] OpenCFD Ltd: Website: www.openfoam.com, [online] https://www.openfoam.com/documentation/guides/latest/doc/guide-applications-solvers-simple.html, 2022. Access on 16.09.2022.

[13] OpenCFD Ltd: Website: www.openfoam.com, [online] https://www.openfoam.com/documentation/guides/latest/api/MPPICFoam_8C.html, 2022. Access on 17.09.2022.

[14] Andrews, M. J.; O´Rourke, P. J.: The Multiphase Particle-In-Cell (MP-PIC) Method for Dense Particulate Flows. Int. J. Multiphase Flow Vol. 22, No. 2, pp.379-402, 1996, 0301-9322(95)00072-0.

[15] Jang, K.; Han, W.; Huh, K. Y.: Simulation of a Moving-Bed Reactor and a Fluidized-Bed Reactor by DPM and MPPIC in OpenFOAM *in* OpenFOAM – Selected Papers of the 11th Workshop. Springer Nature Switzerlang AG, ISBN: 978-3-319-60845-7, 2019.

[16] OpenCFD Ltd: Website: www.openfoam.com, [online] https://www.openfoam.com/documentation/guides/latest/api/classFoam_1_1ErgunWenYuDragForce.html, 2022. Access on 17.09.2022.

[17] Gidaspow, D.; Bezburuah, R.; Ding, J.: Hydrodynamics of Circulating Fluidized Beds: Kinetic Theory Approach. 7th Fluidization Conference, 1992.

[18] OpenCFD Ltd: Website: www.openfoam.com, [online] https://www.openfoam.com/documentation/user-guide/4-mesh-generation-and-conversion/4.4-mesh-generation-with-the-snappyhexmesh-utility, 2022. Access on 20.07.2022.

[19] OpenCFD Ltd: Website: www.openfoam.com, [online] https://www.openfoam.com/documentation/guides/latest/doc/guide-applications-solvers-incompressible-simpleFoam.html, 2018. Access on 21.07.2022.

[20] OpenCFD Ltd: Website: www.openfoam.com, [online] https://www.openfoam.com/documentation/guides/latest/api/ErgunWenYuDragForce_8H_source.html, 2022. Access on 09.09.2022.

[21] OpenCFD Ltd: Website: www.openfoam.com, [online] https://www.openfoam.com/documentation/guides/latest/api/classFoam_1_1ParticleStressModels_1_1HarrisCrighton.html, 2022. Access on 09.09.2022.